

Planet - Disk interaction:
Eccentricity excitation
and orbital evolution

Dissertation

zur Erlangung des Grades eines Doktors
der Naturwissenschaften
der Fakultät für Mathematik und Physik
der Eberhard-Karls-Universität zu Tübingen

vorgelegt von

Gerben Dirksen

aus Vlaardingen (Niederlande)

2006

Tag der mündlichen Prüfung: 14. Juni 2006
Dekan: Prof. Dr. P. Schmid
1. Berichterstatter: Prof. Dr. W. Kley
2. Berichterstatter: Prof. Dr. K. Werner

Hiermit erkläre ich, diese Doktorarbeit selbständig verfaßt und keine anderen als die angegebenen Quellen und Hilfsmittel benutzt zu haben.

Gerben Dirksen

Abstract

This thesis presents the results of numerical simulations on planets embedded in a protoplanetary disk with the hydrodynamics code NIRVANA. We treat the disk as a viscous fluid satisfying the Navier-Stokes equations and integrate these using a finite difference scheme.

We present three sets of calculations. First our participation to the EU code comparison project is described. In this project we compare the results of a test problem relevant to planet formation as calculated by many different codes.

In the second part we investigate a similar problem where we put a 5-Jupiter mass planet into the protoplanetary disk. After several hundred orbits the disk and the gap opened by the planet become eccentric. This periodic state is very robust and can be sustained indefinitely.

Finally we look what happens to the eccentricity of the planetary orbit when the planet is allowed to change its orbit. For small planetary masses for which linear theory may be applied we find a rapid damping of both the eccentricity and inclination. We compare these results to linear theory and find good agreement. For the very massive planets that caused the eccentric disk we find a substantial increase of the eccentricity.

Contents

1	Outline	11
2	Extrasolar planets	13
2.1	Introduction	13
2.2	Detection techniques	14
2.2.1	Direct imaging	14
2.2.2	Radial velocity	15
2.2.3	Photometry	16
2.2.4	Gravitational lensing	17
2.3	Observations of extrasolar planets	18
2.4	Statistics of extrasolar planets	18
2.4.1	Mass function	19
2.4.2	Orbital parameters	20
2.4.3	Host stars	21
2.4.4	Evidence of migration	22
2.5	Observations of planets in protoplanetary disks	22
2.6	Conclusion	23
3	Planet-Disk interaction	25
3.1	Theories of planet formation	25
3.2	Interaction with the disk	26
3.3	Planetary migration	27
3.4	Accretion	28
3.5	Problems	29
3.5.1	Problems with Type I migration	29
3.5.2	Problems with Type II migration	29
3.6	Final remarks	30
4	Numerical method	31
4.1	Hydrodynamics	31
4.1.1	Viscosity	32
4.1.2	Finite difference method	34

4.1.3	Determination of the time step	35
4.2	Orbital motion	35
4.3	Disk planet interaction	36
4.4	Coordinate system	37
4.5	Boundary conditions	38
4.5.1	Boundaries in the angular directions	38
4.5.2	Inner and outer radial boundaries	39
4.6	Model parameters	39
4.7	Some numerical issues	40
4.7.1	Coriolis force	40
4.7.2	Smoothing of the planetary potential	40
4.8	Density floor	42
5	Global disk simulations	43
5.1	The Standard Model	43
5.1.1	Initial Setup: 2D	44
5.1.2	Initial Setup: 3D	44
5.2	EU Comparison project - a test case	45
5.2.1	Initial conditions	46
5.2.2	Jupiter inviscid	47
5.2.3	Jupiter viscous	48
5.2.4	High resolution	49
5.2.5	Neptune inviscid	50
5.2.6	Neptune viscous	51
5.2.7	Conclusions	51
6	Eccentricity excitation in disks	55
6.1	Large planet simulations	55
6.2	The dual-state disk	56
6.3	The eccentric disk	56
6.4	Dependencies on numerical parameters	58
6.5	Dependencies on physical parameters	60
6.6	The two equilibrium states	61
6.7	Eccentricity growth rates	63

6.8	Analysis of one orbit of the eccentric disk	64
6.9	Theoretical analysis	66
6.10	Disk modes	67
6.10.1	Initial eccentric perturbation	68
6.10.2	To first order of the external potential	69
6.10.3	Growth rate of the eccentric mode	71
6.11	Test of the theoretical model	73
6.12	Conclusions	75
7	Simulations with a moving planet	79
7.1	Low mass	79
7.1.1	Initial setup	79
7.1.2	Eccentricity and Inclination damping	80
7.1.3	Numerical setup	81
7.1.4	Low initial eccentricity	81
7.1.5	High initial eccentricity	83
7.1.6	Comparison to two-dimensional models	85
7.1.7	Inclination damping	87
7.2	Eccentric disks and orbital elements	89
7.3	Conclusions	90
8	Conclusions	93
8.1	Fixed planet orbits	93
8.2	Moving planet	94
8.3	Future work	94
9	Curriculum Vitae	106

1 Outline

In this thesis we will discuss the research we have done in the subject of extrasolar planet formation, a subject that has undergone a large expansion in the last few years. The question whether there are planets around other stars has been asked for thousands of years, and in 1995 the first planet orbiting a main sequence star has been found. Since then, over 170 planets around other stars have been found and new discoveries are now made regularly. More and more techniques for finding extrasolar planets are having success and when some planets are observed with different techniques we get more and more information on the system. In Chapter 2 we discuss the history of extrasolar planets and the different methods for detecting an extrasolar planet and their successes.

A planetary system however is only the final product of a formation process, unfortunately the stage where planets are forming from planetesimals cannot be observed directly. It is known that this stage must exist and by carefully studying the known planetary systems and observations of the protoplanetary disks in which planets may be forming we can get a grip on the conditions under which forming planets interact with the protoplanetary disk. From both analytic studies and numerical simulations much has already been learned on the subject of planet-disk interaction. The goal of these studies is to find out how the planets in our Solar System and planets around other stars have formed, what the differences are between our Solar System and extrasolar planetary systems and why these differences exist. In Chapter 3 we summarize the current knowledge of planet-disk interaction.

In this thesis we approach the problem of planet-disk interaction using numerical simulations. We use a finite difference code based on NIRVANA and treat the protoplanetary disk as a viscous fluid. Chapter 4 discusses in detail the numerical methods we use in our code.

To get consistent results from numerical simulations and to be able to trust these results it is important to benchmark one's code. However the standard test problems for numerical codes deal with problems that usually have very different conditions than those of the problem of a protoplanetary disk and an embedded planet. We have participated in a European code comparison project

in which the problem of a massive planet in a protoplanetary disk was studied with many different numerical codes. We discuss our findings for specifically our code in Chapter 5.

Although the planets in the simulations discussed in Chapter 5 move on circular orbits as in our own Solar System, many extrasolar planets move on eccentric orbits. In the next two chapters we look into several mechanisms that could cause an eccentric planetary orbit.

In Chapter 6 we discuss similar simulations as those in Chapter 5 but for planets with masses of 3 to 6 Jupiter masses. We find that for very high mass planets the disk reaches a clearly different equilibrium state than for planets with lower mass. The disk becomes eccentric and this may cause a back reaction on the planet.

To study the effect of the disk on the orbit of the planet in Chapter 7 we allow the planet to change its orbit during the simulation. First in Section 7.1 we study the orbital evolution of a low mass planet embedded in a protoplanetary disk. Since a low mass planet on a circular coplanar orbit will stay on such an orbit we set the eccentricity e and the inclination i nonzero at the start of these simulations and study the evolution of the orbital elements. Then in Section 7.2 we look at the planets studied before in Chapter 6. For the normal equilibrium state we find that a circular orbit remains circular, but for the eccentric equilibrium state eccentricity growth is observed.

Finally in Chapter 8 we list our conclusions and make suggestions on what could have been improved, and what simulations may be done in the future.

2 Extrasolar planets

There are 10^{11} stars in the galaxy. That used to be a huge number. But it's only a hundred billion. It's less than the national deficit! We used to call them astronomical numbers. Now we should call them economical numbers.

- Richard Feynman

This first chapter is intended as a summary of our present knowledge of extrasolar planets at the moment of writing.

2.1 Introduction

All through the history of mankind people have speculated about the possible existence of other worlds. The central theme in this has been whether we are in some way or another unique. In the past many thought that the whole universe revolved around the Earth, but then it turned out that actually the Sun, or more accurately the center of mass of our Solar System, is the center around which the Earth and the other planets revolve. Later it was discovered that the Sun was only one among billions upon billions of stars, and among those a quite ordinary one. It is therefore no surprise that people are wondering whether somewhere out there, there exists a planet similar to Earth.

In 300 BCE the Greek philosopher Epicurus already suggested that there are many other worlds around other suns, perhaps with people on them, asking the same question. However in later times these ideas were out of consideration, at least in Europe, due to the dominance of the Church. However, some still supported this old idea. The Italian scientist Giordano Bruno literally took his life into his hands when he suggested that the stars actually were other suns. In 1600 he was burnt at the stake by the Church for the same suggestion that Epicurus had made almost 2000 years earlier.

The first serious attempts to find planets around other stars were performed in the early 20th century. The motion of Barnard's star, which happens to be the star with the largest proper motion, had been carefully observed for many

years and the conclusion was that there is a planet with a mass of about 1.5 Jupiter masses orbiting this nearby Red Dwarf star (van de Kamp 1963). It is still not clear if this star really has a planet or not. Since to reproduce the data one would have to observe the star over at least one full period of the planet, which allegedly is 25 years. This is naturally very hard to do.

In the late 20th century people recognized that the means to discover planets around other stars were actually there and the first evidence of planets around other stars was found in 1991, when two planets around a pulsar were discovered (Wolszczan 1991). Finally in 1995 the first discovery of a planet around a main sequence star other than our Sun, 51 Pegasi, was made (Mayor et al. 1995).

Little over ten years have past since this discovery at the moment of writing, and now over 170 extrasolar planets are known, the lightest having a mass less than that of Neptune. It will not be long until we can expect the discovery of the first Earth-mass extrasolar planet.

2.2 Detection techniques

There are several possible detection techniques to find planets around other stars, and usually the most simple ideas are not the most successful ones. A tree diagram of the different planet detection methods can be found in Fig. 1. As can be seen some methods are more successful in different mass regimes. We will discuss the most important methods briefly in the following paragraphs.

2.2.1 Direct imaging

This would of course be the first possibility to think of however it turns out to be extremely difficult. To observe Jupiter from the viewpoint of another star is nearly impossible as it would appear to be very close to the Sun with a relative brightness difference of 10^8 between the star and the planet. The problem is two-fold: Since planets are illuminated by their central star, the further they are away from the star the dimmer they are. On the other hand, if they are too close to the star, the light cannot be identified as coming from a different object other than the central star. Presently there have been several reports of a direct image of a planet-sized object around another star, of which GQ Lupi is the

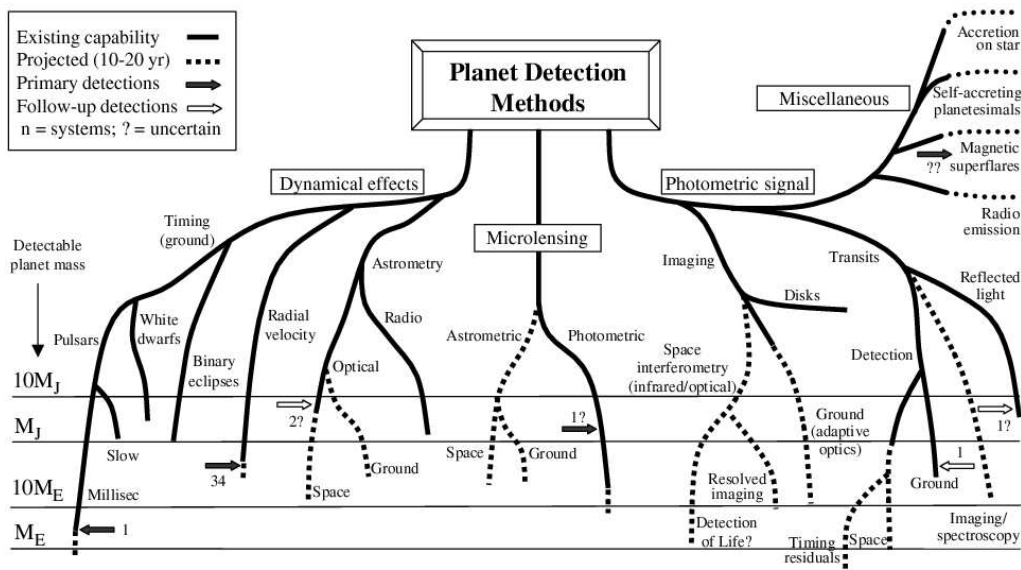


Figure 1: An overview of the different planet detection methods from Perryman (2000). On the vertical axis the current and expected precision of the different methods is shown.

most promising (Neuhäuser et al. 2005), however since one needs to resort to models of young Brown Dwarfs the mass of the object is still subject to debate at the time of writing. As such it is not clear if the companion is a planet or a Brown Dwarf.

2.2.2 Radial velocity

The by far most successful method to detect planets has been the so called radial velocity method. As the planet and the star revolve on their combined center of mass, the host star is moved by the planet and it will show a velocity variation. This velocity variation can be measured in the Doppler shift of the spectral lines of the star. With the combined information from thousands of spectral lines an accuracy of a few m/s can be achieved (Konacki 2005).

As a comparison, the velocity variation of the Sun caused by Jupiter is 12 m/s. However for Jupiter the shift in the spectral lines will be spread out over one orbital period, which in case of Jupiter is about 12 years. Since observations in this area have been taken for about 20 years, people are just finding planets at these distances. On the other hand many planets on shorter period orbits have been found with this method already and this is so far the most

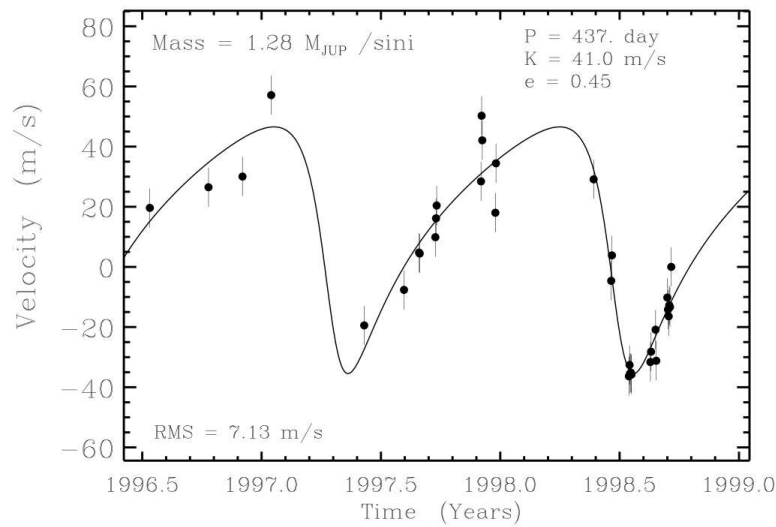


Figure 2: A typical radial velocity curve for the discovery of an extrasolar planet. Plotted is the radial velocity of the star HD 212027 as a function of time with respect to the long-time average and the best-fit Keplerian curve (Marcy et al. 1999).

successful method. As an example observations of the radial velocity of the star HD 212027 are shown in Figure 2.

2.2.3 Photometry

Some planets move in front of their host star to form tiny eclipses. The depth of such an eclipse is about 1% of the total flux from the star for a Jupiter size planet. Because of the geometry, this method favors large planets that are very close to the star. 9 examples of this are known already, the first and most well known of these is HD 209458 (Charbonneau et al. 2000). A typical transit light curve for this planet is shown in Fig. 3.

The great advantage of these transits is most of all a direct measurement of the planet radius as a fraction of the stellar radius. If at the same time a radial velocity is measured one can determine the exact mass of the planet and rule out alternative scenarios, something which is not possible with only radial velocity methods.

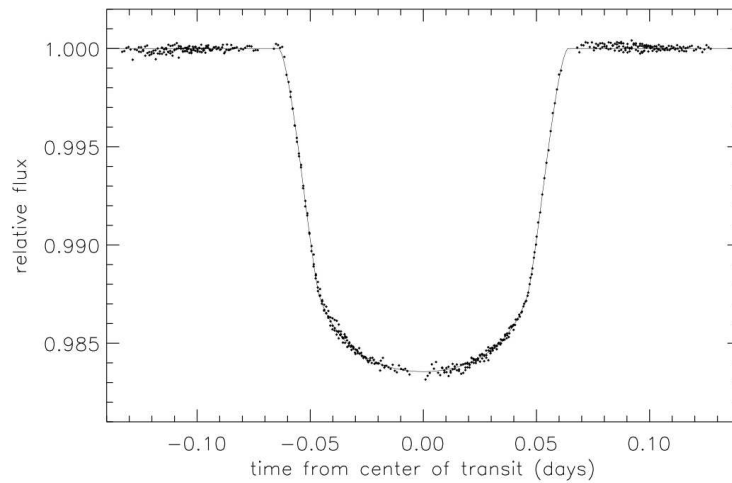


Figure 3: Transit light curve of HD 209458 observed with the STIS spectrograph on the Hubble Space Telescope (Brown et al. 2001).

2.2.4 Gravitational lensing

When two stars align exactly along our line of sight, the light of the background star will be enhanced by gravitational lensing from the foreground star. For a background star near the galactic center and a foreground star somewhere in between, the alignment has to be in the order of a few micro-arc-seconds. This kind of gravitational lensing is called micro-lensing. In the microlensing light curve it is possible to find extra peaks caused by massive companions as these lead to a change of the gravitational lens (Lewis 2001). A planetary companion of the (unseen) foreground star will cause a so-called caustic or curve of infinite magnification, and if the background star moves near this caustic it will cause a temporary extra magnification on top of the magnification of the stellar gravitational lens, and then the planet may be detected. Unfortunately this is a one-time event and can not be repeated on the same star. However if enough observatories register the event it will nevertheless be a well-established observation, and if many of such observations are made one can put constraints on the population of planets orbiting other stars. Additional information on the unseen lens system may be obtained if one waits long enough: The star will move away from the line of sight from the background star to us and may later be detected when the separation is large enough.

This method has the advantage that quite low mass planets can be found, and it is especially sensitive in the semi-major axis range around 1 AU, which makes it a good method to look for Earth-like planets in Earth-like orbits. The first detection of a low mass planet using this method was published in 2005 (Bennett et al. 2005).

2.3 Observations of extrasolar planets

The first success with extrasolar planets around solar type stars was with the radial velocity method. Over 170 planets have been found with this method. An up to date list of the exoplanets discovered with this method is available on the web site of the California & Carnegie Planet Search team ^a. With this method one can determine the orbital period, the eccentricity of the orbit and a minimum estimate of the mass. Not the exact mass can be determined but only the variable $m \sin i$, where i is the inclination of the orbit with respect to the direction of observation. A planetary system that would be seen head-on can not be observed with this method.

HD 209458b was the first planet known to cause a transit of its host star as seen from the Earth (Charbonneau et al. 2000). The combined data from the light curve and the radial velocity measurement give a complete picture of the orbit of the planet. Since the inclination is known to be almost exactly 90° , the mass of the planet is known exactly if we have radial velocity data of the same system. From the depth of the eclipse and stellar models for the physical size of the star one can then determine the diameter of the planet and the exact geometry of the system. A sample high-precision light curve for the star HD209458 is shown in Fig. 3. For the planet HD209458b even a planetary spectrum was measured by comparing the stellar spectra in and out of the eclipse (Fortney et al. 2003).

2.4 Statistics of extrasolar planets

Now that over 170 planets are known, their properties may be analyzed statistically. However because of the observational bias for massive, close in planets we need to always check if the statistic we are studying is not biased.

^a<http://www.exoplanets.org/almanacframe.html>

2.4.1 Mass function

Since for planets discovered with the radial velocity method only $m \sin i$ is known, the planetary mass function is not exactly known. Instead a minimum theoretical mass is observed which is achieved when $\sin i = 1$. The expected actual mass of the planet is on average 20% higher than the observed minimum mass but may exceed this value by a large margin for a face on system. Nevertheless we can make an estimate of the mass function. As can be seen from Figure 6, more planets are found with lower masses. This is not an observational bias. On the contrary, larger mass planets are easier to find. However, since the observations have only been done for about 20 years, we can only say that specific stars have no planets above a specific mass within several AU.

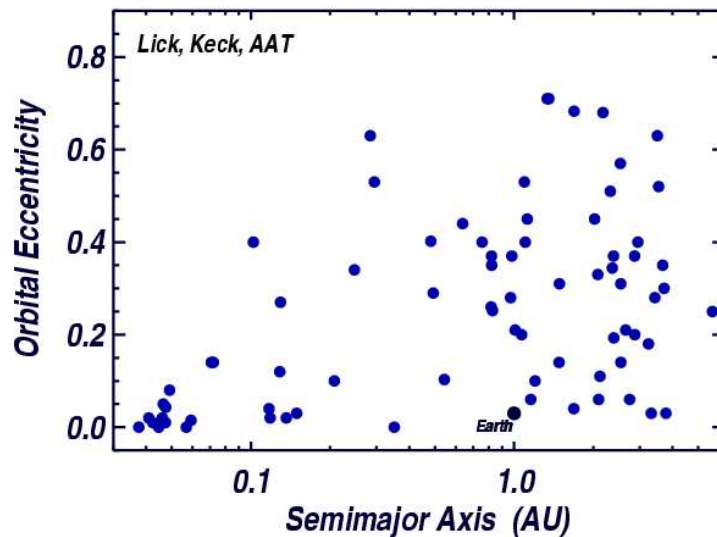


Figure 4: Eccentricity versus semi-major axis for the orbits of the known extrasolar planets (Marcy et al. 2005). The planet responsible for most of the velocity variation of our Sun, Jupiter, would be in the bottom right corner of this plot. The group of points at the bottom left of the diagram are the so-called hot Jupiters: giant planets with an orbital period of less than a week.

If one looks at the complete range of possible companions of a star it is seen that there are two different peaks in mass. One peak for the planetary companions and one peak for the stellar companions. Companions of masses between 10 and 80 Jupiter masses (Brown Dwarfs) are rare; this is called the Brown Dwarf desert. It is not completely empty, but if they were there it

would have been expected that more would have been discovered already with the methods in use.

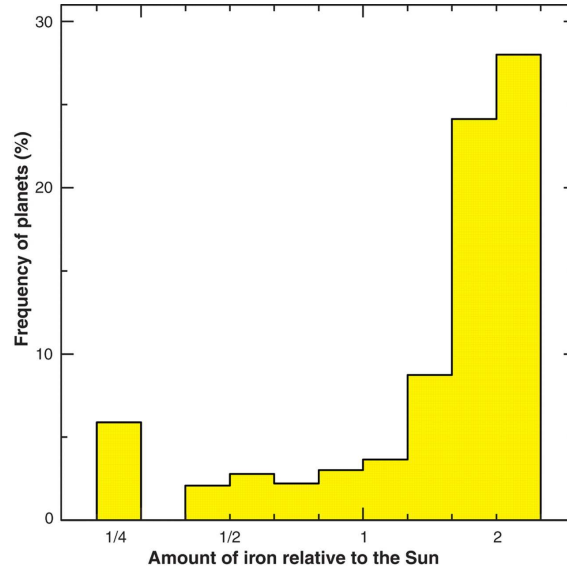


Figure 5: Percentage of stars that were found to have planets as a function of the relative amount of iron with respect to the Sun (Santos et al. 2005).

Not much information is available at the moment of writing of this thesis on the diameters of extrasolar planets. 9 planets have so far been discovered in transiting orbits, and all these planets are quite similar. They have a slightly larger diameter than Jupiter even though their masses are lower than that of Jupiter. There are several models of such planets, see for example Barman et al. (2001).

2.4.2 Orbital parameters

As can be expected from the success of the radial velocity method, more planets have been found on very tight orbits around the host star and only recently planets on wider and wider orbits were found. However it became clear from the beginning that the orbits of extrasolar planets are very different from those in our Solar System: Most planets do not move on nearly circular orbits as in our Solar System, but on moderately up to extremely eccentric orbits. The distribution of orbital eccentricity as a function of semi-major axis is shown in Fig. 4. The group of planets in the bottom left of the graph are Jupiter-type planets in a short-period, tidally circularized orbit. These planets are called hot

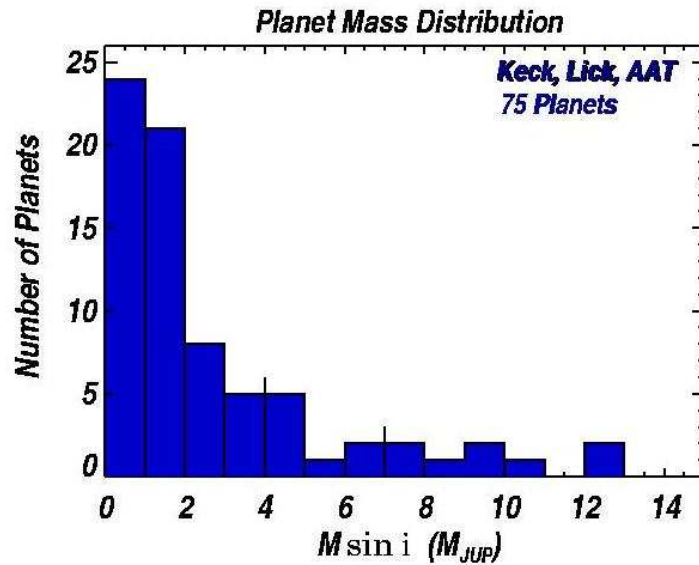


Figure 6: A histogram of the minimum masses of the observed extrasolar planets. There is a trend for more planets at lower masses, which is exactly the opposite of the observational bias as planets with a larger mass are easier to detect (Marcy et al. 2005).

Jupiters.

2.4.3 Host stars

Most host stars to the discovered extrasolar planets are Solar type stars, i.e. low mass Main Sequence stars. Although this is partially caused by the urge to find planetary systems like our own, this also has practical reasons. The radial velocity method, responsible for the vast majority of planet discoveries, is easier to perform on very stable stars that have many spectral lines, which means Solar type stars (Udry et al. 1999). Although a lower precision is reached for more massive stars, the first planets around such stars have been discovered (Setiawan et al. 2005).

One important fact is known however: The abundance of planets as a function of the metallicity of the host star. As can be seen in Fig. 5, with increasing stellar metallicity the chance of finding at least one Jupiter mass planet within 3 AU increases dramatically. This observational fact will need to be present in any theory of planet formation.

2.4.4 Evidence of migration

As will be explained in Chapter 3, when planets are still embedded in a protoplanetary disk they may migrate or in other words change their orbital parameters. Although planetary migration is not observed directly as planets have only been found in systems without a disk, the final results of migration are readily observed. First there is the existence of the hot Jupiters. These heavy planets could not have formed at this location so some mechanism must have brought them where they are now. The most likely explanation is interaction with a protoplanetary disk. Another sign of migration is the existence of multiple planet systems where the planets are in orbital resonance, that is their orbital periods compare to each other with small integers. An example is the system Gliese 876, where two large planets orbit their central star in orbits of 30 and 60 days, i.e. a 2:1 resonance (Marcy et al. 2001). To infer the correct orbital elements for the two strongly interacting planets, a 3-body problem has to be solved. If one would not do this, the resulting effect may well be mistaken for a third massive planet in the system.

2.5 Observations of planets in protoplanetary disks

There have been many observations of protoplanetary disks, that is of disks that are assumed to have formed or that are presently forming planets. However the inner region, closer than 20 AU from the star, where the planets actually form cannot be observed directly. Since this region is relevant for our calculations it is important to know the conditions there. Unfortunately not much is known.

The inner region can be explored indirectly by taking a spectrum of the nebula in the infra-red regime. Especially with the Spitzer satellite (Muzerolle et al. 2004) that was especially designed for this purpose there have been some important results. In many young systems there was evidence for grain growth, essential to at least start the process of planet formation (Kessler-Silacci and C2d Irs Team 2005). In some systems there is evidence for an inner gap in the disk (Malbet et al. 2000) which suggests there may be a large planet in the gap, forcing the disk material to stay outside a certain radius from the star. Direct evidence of a planet embedded in a planetary disk is still not found.

2.6 Conclusion

In the past decade, the field of extrasolar planets has become a very rich one, with many successful techniques to find new planets. It is now up to the theorists to make models that will both explain our own Solar System as well as the many new found systems around other stars. On the observing side there is still much promise for the future: People are actively thinking of ways and building instruments that will lead to the discovery of a second Earth. Some of the most promising projects in this respect are the GAIA (Crifo and The Gaia Team 2004) and DARWIN (Fridlund and Capaccioni 2002) missions.

3 Planet-Disk interaction

We are just an advanced breed of monkeys on a minor planet of a very average star. But we can understand the Universe. That makes us something very special.

- Stephen Hawking

3.1 Theories of planet formation

Although we have known for a long time that planets form from protoplanetary disks, see for example Berlage (1934), before 1995 there was only one system to base our theories on. Since then the old formation scenario has come under discussion and in the least needs some fixes to account for the wide range of systems discussed in the previous Chapter. At the moment there are basically two main scenarios for giant planet formation in these disks. The first possibility is that planets form by a gravitational instability in the protoplanetary disk (Boss 1999). The disk will fragment and these fragments will form planets. The problems with this theory are that it is hard to form planets with a mass below $1 M_{Jup}$, and that the conditions for gravitational instability require efficient cooling of the protoplanetary disk.

The second theory is that planets form by core accretion, see for example Mizuno (1980). The core of giant planets grow from micron size particles up to several Earth masses (Hartmann 1968), and then they attract the gas gravitationally to grow to Jupiter size (Lissauer and Stewart 1991). There are also several problems with this theory. One is that it takes about the same time to form large planets this way compared to the life time of the disk, which is estimated to be of the order of 10^7 years based on observations of gas or lack of gas in protoplanetary disks of different ages (Bally et al. 1998). Another problem is that planets of several Earth masses migrate so quickly into the central star that we might not have any left. More on this in section 3.5.1.

3.2 Interaction with the disk

As we have seen in section 2.4.4, an embedded planet interacts with the protoplanetary disk it is forming in. The planet accretes matter from the disk to increase its mass. To form our Solar System a minimum amount of gas and dust was needed, and the lightest possible protoplanetary disk around the Sun defines the Minimum Mass Solar Nebula, MMSN for short (Kargel 1987). On the other hand the planet also interacts gravitationally with the disk. The planetary potential will change the mass distribution of the disk and in return the mass fluctuations will cause a net torque on the planet. This net torque will cause the planet to migrate. The study of the interaction between the planet and the protoplanetary disk has become a rapidly expanding field in the last decade and much work is done in this subject.

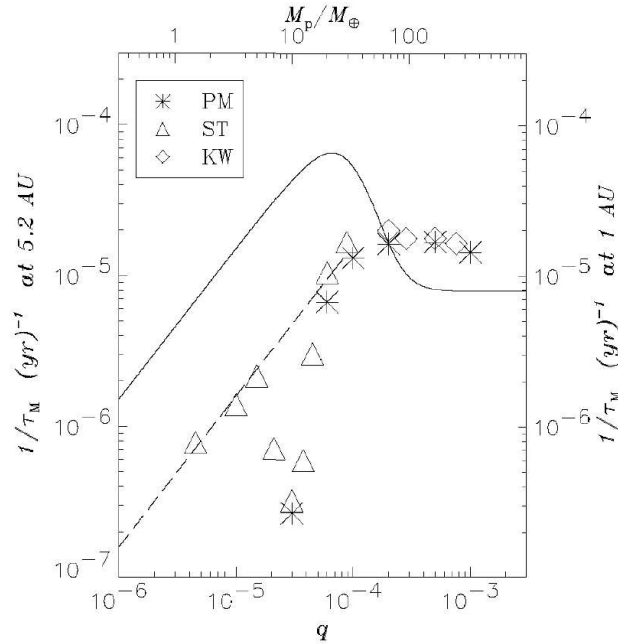


Figure 7: The migration rate as a function of planetary mass for a disk mass of the Minimum Mass Solar Nebula. The lines are theoretical models from Ward (1997) (solid line) and Tanaka et al. (2002) (dashed line). The different symbols are different models as discussed in D'Angelo et al. (2002).

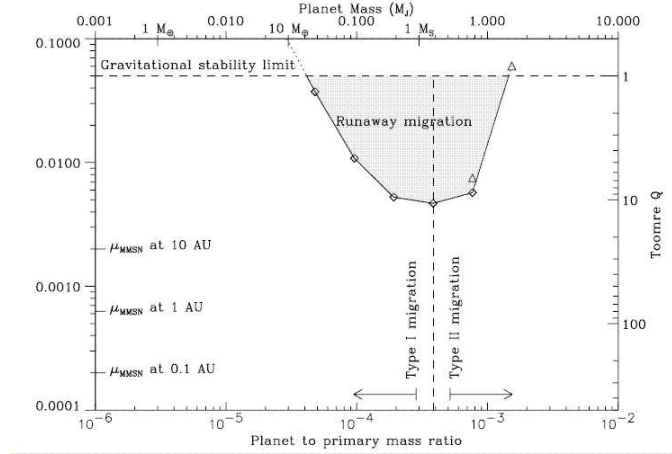


Figure 8: The regimes for the different types of migration as a function of planet and disk mass (Masset and Papaloizou 2003). Low mass planets undergo Type I migration, high mass planets undergo Type II migration, but in the intermediate mass range and high disk masses the Type III migration or runaway migration may be at work. The planet orbit can change very rapidly in this regime.

3.3 Planetary migration

The net torque from the disk onto the planet from the protoplanet is different in different planetary mass regimes. For sufficiently small planets one can make an analytical estimate of the torque and from that calculate the migration rate by treating the planet (Ward 1981) as a perturbation and then applying linear theory. This is called type I migration. Numerical simulations have been performed to verify the validity of the approximation, for example by D'Angelo et al. (2002).

Sufficiently large protoplanets will create a ring-shaped mass-depleted region along its orbit called the gap (Kley 1999). Gap-opening planets have a migration rate which is very different from the linear approximation given above. Because of the gap, the disk is divided up into two physically disconnected parts, and the planet is forced to move with the viscous accretion of the disk. This is called Type II migration, see for example Masset and Papaloizou (2003). To see the migration rate as a function of time as calculated theoretically and by numerical integrations, see Fig. 7. In this figure the migration rate \dot{a}/a is plotted as function of the mass ratio between the planet and the star q . As can be seen in the figure, for planets up to a mass ratio of $q = 10^{-5}$ good agreement to the linear theory is found. Also the constant migration rate

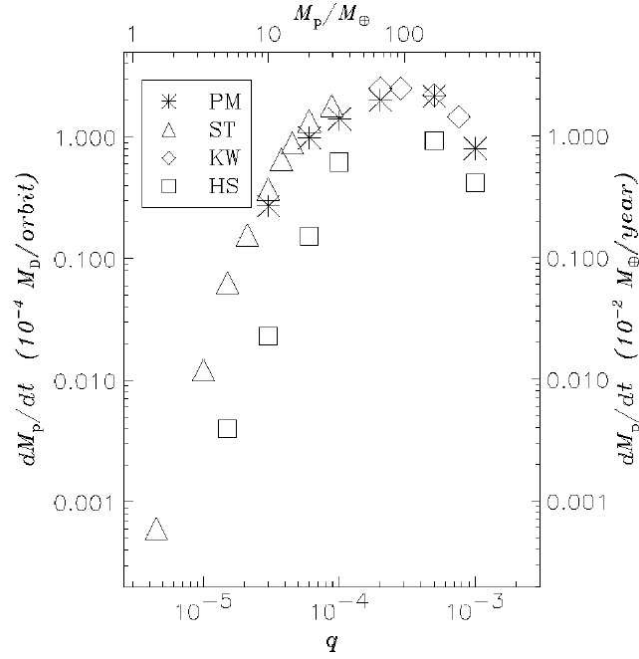


Figure 9: The accretion rate as a function of planetary mass for a MMSN disk. Up to about Jupiter masses the accretion rate increases, but as soon as a gap is opened in the disk the accretion rate starts to decrease for higher planet masses. The different symbols are different models as discussed in D’Angelo et al. (2002) and correspond to the symbols used in 7.

for large planet is reproduced. However the mass regime between these two extremes is not well understood and subject to debate.

There is also a third type of migration, aptly called Type III migration, which is valid for a massive disk and a planet that is approximately between the mass ranges of Type I and Type II migration. At this stage the planet is very mobile and may migrate very quickly through the disk. It is caused by an imbalance in the torques of material that is in corotation of the planet, the so-called corotational torques (Masset 2001). In Figure 8 the different migration regimes are shown as a function of planet mass and disk mass.

3.4 Accretion

The accretion rate onto a planet is essential for the time scale on which large planets may form. First of all the planet needs to be formed completely during the lifetime of the disk, which is approximately 10^7 years, see for example Takeuchi et al. (2005). Once the disk is gone, the planet can no longer grow.

Especially for very massive planets this is a problem. As soon as the planet opens a gap in the disk, accretion slows down. For planets that are larger than several Jupiter masses, time is really short to form them in time.

Also at any point during its growth the accretion timescale must be shorter than the migration time scale, otherwise the planet will not grow and migrate into the central star. D'Angelo et al. (2002) have performed numerical simulations in which they measured the migration rate for different planet masses. The migration rate as a function of planet mass is shown in Fig. 9.

3.5 Problems

There are many unsolved problems in the area of planet-disk interaction and this thesis is intended as a small piece in the quite large puzzle. Here are some of the problems with both Type I and Type II migration.

3.5.1 Problems with Type I migration

Type I migration can be very fast, indeed faster than the mass accretion rate onto the planet. This means that for a planet to survive it must be saved from falling into the central star. This is a serious problem and some ideas to solve this have been suggested in Nelson and Papaloizou (2004). If there is a magnetic field in the disk this will be a source of turbulence. This turbulence will then change the fast inward migration into a random walk, and in this way some planets will be able to survive up to the point where they open a gap in the disk.

3.5.2 Problems with Type II migration

Also for Type II migration there are some problems. There are a lot of planets that are orbiting on very close orbits, with periods of only a few days. It is not clear how these planets stopped migrating into the central star, and if all massive planets migrated, why is our Jupiter so far away from the Sun?

Also for the largest planets there is a problem with the accretion rate. As can be seen in Fig. 9 the accretion rate starts to decrease when Jupiter mass is reached, however this is where it is needed most, as planets have been observed

with masses to over 10 Jupiter masses. At this point the total time to form a giant planet starts to exceed the life time of a protoplanetary disk.

3.6 Final remarks

Also since most of the extrasolar planets are on eccentric orbits, is it possible to excite eccentricity in the accretion phase or do other effects have to account for this? And again the question is, why were these forces not at work in our own Solar System?

Some of the above problems will be addressed by numerical simulations of embedded planets in disks in this thesis.

4 Numerical method

It would appear that we have reached the limits of what it is possible to achieve with computer technology, although one should be careful with such statements, as they tend to sound pretty silly in 5 years.

- John von Neumann, 1949

To approach the problem of a planet in a disk we use a computer code based on NIRVANA (Ziegler 1998). The methods used are similar to the ZEUS code (Stone and Norman 1992). It is a finite difference code which means that physical variables are stored at a pre-defined set of fixed points. Then using the evolution equations these variables are then evolved in time. This way the initial conditions of the studied physical system are evolved and the state of the system at a later point in time is calculated.

In this code the protoplanetary disk is treated as a viscous fluid with the Navier-Stokes equations as the equations of motion. The planet moves on a Keplerian orbit, which in some simulations may be perturbed by the gravitational force of the disk onto the planet.

4.1 Hydrodynamics

A protoplanetary disk consists mostly of gas and dust. However in the phase of evolution of the system that we are looking at, where a large planet has already formed, the gas and dust have decoupled and most of the dust has already formed larger bodies that do not interfere or collide with the planet. Hence, only the gas is considered and this is treated as a viscous fluid, satisfying the equations of hydrodynamics. These equations deal with 6 variables: Three scalar variables (density ρ , pressure P and temperature T) and the velocity vector \mathbf{v} . To close the system we need 6 equations. Five of these are given by conservation laws.

Conservation of mass:

$$\frac{\partial \rho}{\partial t} + \nabla \cdot (\rho \mathbf{u}) = 0 \quad (4.1)$$

ρ is the local density of the gas and \mathbf{u} is the local velocity vector of the gas.

Conservation of momentum:

$$\frac{\partial \rho \mathbf{u}}{\partial t} + \nabla \cdot (\rho \mathbf{u} \otimes \mathbf{u}) = -\nabla p + \rho \mathbf{k} + \nabla \cdot \underline{\underline{\sigma}} \quad (4.2)$$

\mathbf{k} are the specific external forces, i.e. force per unit mass, in our case the gravitational forces of the planet and the central star. In the code these forces are treated as an external potential Φ . σ is the viscous stress tensor and will be discussed in section 4.1.1. p is the local gas pressure. \otimes denotes the tensor product of two vectors: $(a \otimes b)_{ij} = a_i b_j$

Conservation of energy:

$$\frac{\partial \rho \epsilon_{tot}}{\partial t} + \nabla \cdot (\rho \epsilon_{tot} \mathbf{u}) = -\nabla \cdot p \mathbf{u} + \nabla \cdot (\mathbf{u} \cdot \underline{\underline{\sigma}}) - \nabla \cdot F + \rho \mathbf{u} \cdot \mathbf{k} \quad (4.3)$$

where ϵ_{tot} is the specific total energy of the system and F the external energy flow. Disk self-gravity is neglected in these simulations.

To close the system of equations we need also an equation of state for the gas:

$$p = p(\rho, \epsilon) \quad (4.4)$$

In our model we use the equation of state of an ideal gas:

$$p = R\rho T/\mu \quad (4.5)$$

where μ is the mean molecular weight of the gas and R the universal gas constant. In a disk column in thermodynamic equilibrium this defines a local disk scale height H . In our model we specify the temperature $T = T_0 r_0/r$, which has the effect that the effective scale height H/r is constant over the whole disk and no energy equation needs to be solved.

4.1.1 Viscosity

In a protoplanetary disk we need a non-vanishing effective viscosity. This can readily be seen when we look at our own solar system. In our Solar System, over 99% of the mass is concentrated in the Sun and over 99% of the angular momentum is concentrated in the planets. To reach this state there must have been a transfer mechanism that transported mass inward and angular momentum outward. This process is called turbulent accretion.

However, the molecular viscosity of the gas and dust in the disk is insufficient to explain the short life time of a protoplanetary disk, which is approximately 10^7 years. There must be a different cause of the viscous accretion.

For the moment we will just assume that such a viscosity exists and define the viscous stress tensor σ :

$$\sigma_{ij} = \eta \left[\left(\frac{\partial u_i}{\partial x_j} + \frac{\partial u_j}{\partial x_i} \right) - \frac{2}{3} \nabla \cdot \mathbf{u} \delta_{ij} \right] \quad (4.6)$$

The term responsible for viscous accretion in protoplanetary disks is $\sigma_{r\varphi}$. In many calculations the simple ansatz is made to assume the viscosity is of the form

$$\eta = \alpha \rho c_s^2 \quad (4.7)$$

where α is a constant smaller than one, and c_s the local sound speed, given by

$$c_s^2 = p/\rho = \frac{H}{r} v_{Kepler} \quad (4.8)$$

Such a model is called an α -disk model and is described in more detail in Balbus and Hawley (1991). In our calculations the full stress tensor is used. To define the amount of viscosity in the system we set the kinematic viscosity $\nu = \eta/\rho$ as a constant.

The main model to explain effective mass and angular momentum transport in the disk is the Magneto-Rotational-Instability, MRI for short (Balbus and Hawley 1991). It is present if there is a magnetic field in a disk where material further out is rotating slower than material further in, which is the case in a protoplanetary disk, which velocity profile is close to Keplerian. A possible cause of the magnetic field may be ionization of the gas in the disk, however it is not clear if this is present.

The MRI causes turbulence which can be seen as an active viscous term (Papaloizou and Nelson 2003). However it is too time-consuming to model this effect for our calculations, so a shortcut is to assume that the viscosity is of a certain form as given by Equation 4.7.

In our dimensionless units we set the kinematic viscosity to $\nu = 10^{-5}$. For a Minimum Mass Solar Nebula (MMSN) and the embedded planet with a semi-

major axis of $a = 5$ AU this corresponds to $\nu = 10^{10} \text{m}^2/\text{s}$, consistent with the measured accretion rates in protoplanetary disks (Henning and Ilgner 2003).

To compare our simulations to the α -disk models we find from the different definitions that

$$\nu = 2/3\alpha c_s H \quad (4.9)$$

which means that the viscosity in our simulations corresponds to an α -value of several times 10^{-3} .

4.1.2 Finite difference method

These equations are now evaluated in a domain that is divided into grid cells. In spherical coordinates the scalar physical parameters ρ , p , T are defined at the centers of each cell at coordinates $(x_i, y_j, z_k, i = 1..N_x, j = 1..N_y, k = 1..N_z)$. The velocity and first derivatives of the scalar physical parameters are defined on the cell interfaces: in 3 dimensions this is at the center of the faces a cube (see Figure 4.1.2). Now the system is evolved for one time step in all (two or three) directions separately and new values for the physical parameters are found.

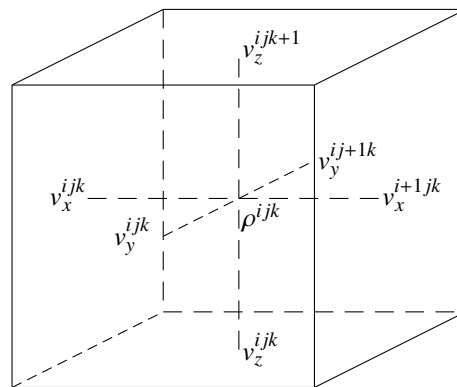


Figure 10: The location of the different variables in a grid cell. The scalar variables are defined at the cell center, vector variables at the cell faces.

4.1.3 Determination of the time step

To determine how large a time step can be taken the Courant-Friedrich-Levy (CFL) criterion is used:

$$\Delta t < CFL \cdot \min \left(\frac{\Delta r_i}{\mathbf{u}_i + c_s} \right) \quad (4.10)$$

where the minimum is over all grid cells and directions and CFL is a constant parameter which is chosen in relation to the numerical scheme used. This parameter has been chosen as $\frac{1}{2}$ in most calculations. The CFL criterion for the time step makes sure that no information moves more than the distance of a cell during one time step so that the local approach is justified.

4.2 Orbital motion

The planet and the central star are on Keplerian orbits, possibly perturbed by the gravitational force of the disk onto the planet and the star. To solve Newton's equations for an N-body system a fourth order Runge-Kutta scheme is used for the forces of the disk and the planet, and if the planet orbit is allowed to change, the disk is added in first order as a small perturbation. The method as we use it in more detail is as follows:

First consider the actual state of the system of N bodies at time t : $\mathbf{r}_i(t), \mathbf{v}_i(t), i = 1 \dots N$. The new state of a body is given as a function of the acceleration by the other massive bodies:

$$\ddot{\mathbf{r}}_{i,grav} = - \sum_{j \neq i}^N \frac{GM_j \mathbf{r}_{ij}}{|\mathbf{r}_{ij}|^3} \quad (4.11)$$

where $\mathbf{r}_{ij} = \mathbf{r}_i - \mathbf{r}_j$ is the vector pointing from body i to body j .

This whole system can be written as a set of first order differential equations:

$$\dot{\mathbf{r}}_i = \mathbf{v}_i, \dot{\mathbf{v}}_i = - \sum_{j \neq i}^N \frac{GM_j \mathbf{r}_{ij}}{|\mathbf{r}_{ij}|^3} \quad (4.12)$$

In 3 dimensions, this gives a 6N-dimensional system of the general form:

$$\dot{\mathbf{y}} = f(t, \mathbf{y}) \quad (4.13)$$

This formula is then discretized using the following 4th order Runge Kutta scheme:

$$y_{n+1} = y_n + \frac{1}{6}k_1 + \frac{1}{3}k_2 + \frac{1}{3}k_3 + \frac{1}{6}k_4 + O(\Delta t^5) \quad (4.14)$$

where the subscript n denotes the number of the current time step and the four k 's are defined as:

$$\begin{aligned} k_1 &= \delta t f(t_n, y_n) \\ k_2 &= \delta t f\left(t_n + \frac{1}{2}\delta t, y_n + \frac{1}{2}k_1\right) \\ k_3 &= \delta t f\left(t_n + \frac{1}{2}\delta t, y_n + \frac{1}{2}k_2\right) \\ k_4 &= \delta t f(t_n + \delta t, y_n + k_3) \end{aligned}$$

One implementation of this method, as used in the code, is known as RK4 (Press et al. 1992, see). A test with a standard 2-body system has shown that the relative energy loss of this method with the actual time step used (as we will see later this is about 0.001 times the orbital period) over the length of a typical simulation is of the order 10^{-6} and can be neglected.

4.3 Disk planet interaction

The motion of the star and the planet in their orbit are given by the gravitational force on the i^{th} body from the other bodies and the disk:

$$\dot{\mathbf{u}}_i = - \sum_{j \neq i} \frac{GM_j \mathbf{r}_{ij}}{r_{ij}^3} - \int_V \frac{G\rho \mathbf{r}}{r^3} dV \quad (4.15)$$

Since the motion is heavily dominated by the 2-body motion between the star and the planet, we can speak of orbital elements of the planet:

- a Semi-major axis
- e Eccentricity
- i Inclination
- ψ Longitude of ascending node
- ϖ Longitude of perihelion
- M Mean longitude

These will change slowly in time as the 2-body system is perturbed by the disk, more precisely if we write the force by the disk onto the planet as F_r, F_z, F_φ in a local (Hill) approximation we will get:

$$da/dt = \frac{1}{M_p \Omega_p a} 2F_\varphi \quad (4.16)$$

$$de/dt = \frac{1}{M_p \Omega_p a} [F_r \sin(\Omega_p t - \varpi) + 2F_\varphi \cos(\Omega_p t - \varpi)] \quad (4.17)$$

$$di/dt = \frac{1}{M_p \Omega_p a} F_z \cos(\Omega_p t - \psi) \quad (4.18)$$

$$d\psi/dt = \frac{1}{M_p \Omega_p a} F_z \sin(\Omega_p t - \psi) \quad (4.19)$$

$$d\varpi/dt = \frac{1}{M_p \Omega_p a} [-F_r \cos(\Omega_p t - \varpi) + 2F_\varphi \sin(\Omega_p t - \varpi)] \quad (4.20)$$

See for example Nakazawa and Ida (1988).

In the code this force is considered small relative to the gravitational forces from the different massive bodies and is considered only once per time step. It is added as a term $k_5 = \delta t f_{disk}(t_n, y_n)$

in the Runge-Kutta scheme described in the previous paragraph.

For the opposite force from the massive bodies onto the disk the gravitational potential is directly inserted into the hydrodynamical equations. Since this is not completely straightforward, check the section on numerical issues (Section 4.7) for more detail.

4.4 Coordinate system

In our calculations we use a cylindrical coordinate system (r, φ) for two-dimensional calculations and a spherical coordinate system (r, θ, φ) for three-dimensional calculations, where the origin of the coordinate system is the center of mass of the planet and the star. In this coordinate system the computational domain is defined as a box where each coordinate x runs from x_{min} to x_{max} .

The coordinate system is rotating with a constant rate Ω which corresponds to the orbital period of the planet. These coordinates are very suitable for the problem since the central star can be left outside of the grid and the planet is on a fixed location on the grid (or moves around only slightly if it revolves on an eccentric or inclined orbit). The grid covers the full domain $[0, 2\pi]$ in

the φ -direction and has fixed boundaries in the other one or two directions. To keep the planet away from the grid boundary at $\varphi = 0$ it is kept at $r = 1, \varphi = \pi$ if it is not allowed to move, or near to this point if it is.

In the code the computational domain is divided into cells, and in each direction the interval $[x_{min}, x_{max}]$ is divided into N_x smaller intervals of step size Δx . Since there are distinct staggered grids where the different variables are defined we distinguish between physical variables defined in the center of the cells at coordinate point x_i , and physical variables defined at the cell interfaces at coordinate point $x_{i+\frac{1}{2}}$. The effective physical borders of the computational domain in a given coordinate direction are $x_{min} = x_{\frac{1}{2}} = x_1 - \frac{1}{2}\Delta x$ and $x_{max} = x_{N+\frac{1}{2}}$.

4.5 Boundary conditions

To ensure the correct physical evolution of the system at the boundaries, two rows of ghost cells are included on each border of the computational domain. In these ghost cells the physical variables are defined but not numerically evolved. After each routine in the code that may have changed the values of the physical variables near the boundary, the values in the ghost cells will be redefined accordingly, depending on the chosen boundary conditions.

4.5.1 Boundaries in the angular directions

In the φ -direction the computational domain should be periodic. To ensure this, the values of the physical variables are simply copied from the actual values from the other side of the grid ($X_{N+1} = X_1, X_{N+2} = X_2, X_0 = X_N, X_{-1} = X_{N-1}$). These boundary conditions are called "periodic" boundary conditions.

In the θ -direction in three-dimensional calculations normally "reflecting" boundary conditions are used: material is not allowed to escape. As the density is very low in this region there is not much trouble with wave reflections. In three-dimensional calculations that would lead to a vertically symmetric system, half of the computational time is spared and the boundary of the computational domain is at the mid plane. At this point, the values of the physical variables in the first ghost region will be the same as in the first real cell ($X_0 = X_1$), and the physical variables in the second ghost region will be the

same as in the second real cell ($X_{-1} = X_2$). These boundary conditions are known as "symmetric" boundary conditions.

4.5.2 Inner and outer radial boundaries

In principle two options stand out here. Either outflow of material is allowed or it is not. If it is, the gas in the inner disk will disappear into the inner boundary too quickly due to both viscosity and the spiral waves caused by the planet. If outflow is not allowed (reflecting boundary conditions), waves will collide with the boundary and get reflected.

To ensure a most uniform environment for all models and minimize disturbances (wave reflections) from the inner and outer boundary we impose at r_{\min} and r_{\max} damping boundary conditions where the density and both velocity components are relaxed towards their initial values as

$$\frac{dX}{dt} = -\frac{X - X(t=0)}{\tau_{\text{damp}}} R(r)^2 \quad (4.21)$$

where $X \in \{\Sigma, u_r, u_\varphi\}$, $\tau_{\text{damp}} = 1/\Omega_{\text{K}}(r_{\text{boundary}})$ and $R(r)$ is a dimensionless linear ramp-function which is one at the domain boundary and zero at the interior boundary of the wave killing zone. The wave killing zone at the inner boundary is the radial range $[0.4, 0.5]$, the wave killing zone at the outer boundary is of the form $[0.84r_{\max}, r_{\max}]$. This damping setup has been defined in the international comparison test project^b.

The initial radial velocity vanishes, and the boundary conditions ensure that no mass flows through the radial boundaries at r_{\min} and r_{\max} . However, the total mass in the system may nevertheless vary due to the applied damping.

These specific boundary conditions allow upon a long term evolution and, if the planet is on a fixed orbit, will lead to a well defined stationary or, as we will see, periodic state.

4.6 Model parameters

The computational domain is covered by 128×384 ($N_r \times N_\varphi$) grid cells for the smaller models $[0.4, 2.5]$ and 200×384 for the larger $[0.4, 4.0]$ runs. Three-dimensional runs have 16 cells in the vertical direction and make use of mirror

^b<http://www.astro.su.se/~pawel/planets/test.hydro.html>

symmetry in the orbital plane and cover 4 scale heights. The grid is spaced equidistantly in all directions. The inner radius beyond which the damping procedure defined above gradually sets in is given by $r_{\text{damp}} = 0.5$, the outer damping radius is given by $R_{\text{damp}} = 0.84r_{\text{max}}$. The star has a mass of $1 M_{\odot}$, and the mass of the planet in the different models ranges from one to five Jupiter masses. The planet is held on a fixed circular orbit.

For the viscosity a value of $\nu = 1.0 \cdot 10^{-5}$ (in units of $\Omega_p r_p^2$) is used for our standard models, which is equivalent to a value of $\alpha = 0.004$ for the standard $H/r = 0.05$. This is a typical value for the effective viscosity in a protoplanetary disk.

To achieve a more detailed calculation of the observed phenomena we refined some calculations to the higher resolution of 256×768 ($N_r \times N_{\varphi}$) by interpolating the data from coarser calculations. As the relaxation time for the system is very long (> 1000 orbits) it would be too time-consuming to complete the whole calculation on the high-resolution grid. To study the influence of physical parameters such as viscosity and pressure, we vary ν and H/r in some models. In addition, we analyze the influence of several numerical parameters on the results.

4.7 Some numerical issues

4.7.1 Coriolis force

The use of a rotating coordinate system requires special treatment of the Coriolis terms to ensure angular momentum conservation (Kley 1998). Especially for the long-term calculations presented here, this is an important issue.

4.7.2 Smoothing of the planetary potential

In calculating the gravitational potential of the planet we use a smoothed potential of the form

$$\Phi_p = -\frac{GM_p}{\sqrt{R^2 + \epsilon^2}} \quad (4.22)$$

where R is the 2-dimensional distance from the planet. For the smoothing length of the potential we choose $\epsilon = 0.6H$ for 2-dimensional calculations and the diagonal size of a grid cell in 3-dimensional calculations. The increased

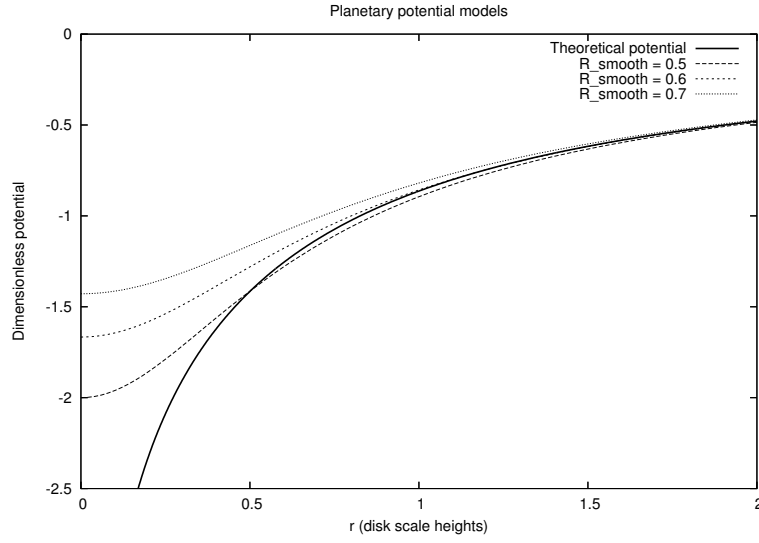


Figure 11: The vertically integrated theoretical potential of a planet on a 3-dimensional disk in a 2-dimensional simulation (solid line) and 3 potentials with a fixed smoothing length. As can be seen in the outer regions the potential with a smoothing length of $0.6H$ is the best fit. In the inner region this potential is continued as the theoretical potential is too steep and may lead to numerical artifacts..

smoothing length is to simulate a three-dimensional disk in a two-dimensional calculation. The gravitational force from the disk onto the planet (and vice versa) is overestimated for distances that are not large compared to the scale height of the disk. The horizontal component of the gravitational force from disk elements outside of the orbital plane only contribute to the horizontal component with a factor $\cos(\alpha)$, where α is the angle between the line from the planet and the disk element and the orbital plane.

The vertically integrated force of the disk onto the planet gives this formula:

$$F_{th}(R) = \int_{-\infty}^{\infty} \frac{Re^{\frac{-z^2}{2H^2}}}{(R^2 + z^2)^{3/2}} dz \quad (4.23)$$

Since the force from the planet onto the disk will be the exact opposite, this defines a planet potential that can be found by integrating this force. As there is no analytic formula for this potential and many use a smoothed potential of the form Φ_P , we chose the value of ϵ that gave the potential most similar to the theoretically correct model. In Figure 11 the theoretical 2-dimensional

potential Φ_{th} defined by

$$\Phi_{th}(R) = \int_R^{\infty} F_{th}(R') dR' \quad (4.24)$$

is compared to the potential Φ_P for different values of the smoothing length. As can be seen from the Figure the value $\epsilon = 0.6H$ gives the best fit to the theoretical potential for regions far away from the planet.

For 3D calculations we use the same formula for smoothing the planetary potential but with a different value of ϵ and for a completely different reason. If no smoothing is used at all the large potential gradient near the planet will cause a-physical results. To counter this we use a potential smoothing of one diagonal grid cell measured at the location of the planet ($\epsilon = \sqrt{\Delta r^2 + \Delta \theta^2 + \Delta \varphi^2}$).

4.8 Density floor

As the planet can be very large and as such cause a very deep gap, we have found it preferable to work with a density floor so that the density cannot fall below a specified minimum value Σ_{\min} . For our purpose we use a value of $\Sigma_{\min} = 10^{-6}$ in dimensionless values, where the initial density is of $O(1)$.

5 Global disk simulations

Science is wonderfully equipped to answer the question "How?" but it gets terribly confused when you ask the question "Why?"

- Erwin Chargaff

This chapter discusses general simulations of a protoplanetary disk with an embedded planet and especially the EU test project.

5.1 The Standard Model

Numerical simulations are an important tool to tackle the problems in the theory of planet-disk interaction described in Chapter 3. Since the interaction between a forming planet and a protoplanetary disk can not be observed directly we have to resort to models and then compare the final state reached in these models with the observed planetary systems. In doing so we have to take into account the limits on the initial conditions of planet formation put on us from observations of protoplanetary disks.

The models presented here are calculated basically in the same manner as those described previously in Kley (1998, 1999) and in Chapter 4.

Other similar models, following explicitly the motion of single planets in disks, have been presented by Nelson et al. (2000), Bryden et al. (2000).

We use cylindrical coordinates (r, φ, z) and consider a vertically averaged, infinitesimally thin disk located at $z = 0$. The origin of the coordinate system, which is co-rotating with the planet, is at the combined center of mass of star and planet. The basic hydrodynamic equations (mass and momentum conservation) describing the time evolution of such a viscous two-dimensional disk with embedded planets have been stated frequently and are not repeated here (see Kley 1999).

In the present study we restrict ourselves to the situation where the embedded planet is on a fixed orbit, i.e. the gravitational back reaction of the disk on the planet is not taken into account.

5.1.1 Initial Setup: 2D

The two-dimensional ($r - \varphi$) computational domain consists of a complete ring of the protoplanetary disk. The radial extent of the computational domain (ranging from r_{\min} to r_{\max}) is taken such that there is enough space on both sides of the planet, although, as we shall see later, the effect we are analyzing appears to occur only in the outer disk. Typically, we assume $r_{\min} = 0.40$ and for r_{\max} we take two different values: 2.5 and 4.0, in units where the planet is located at $r = 1$. In the azimuthal direction for a complete annulus we have $\varphi_{\min} = 0$ and $\varphi_{\max} = 2\pi$.

The initial hydrodynamic structure of the disk (density, temperature, velocity) is axisymmetric with respect to the location of the star. The surface density is constant ($\Sigma = 1$ in dimensionless units) over the entire domain with no initial gap. To make sure that only little disturbances or numerical artifacts arise upon immersion of the planet, its mass will be slowly turned on from zero to the final required mass (e.g.. 5 Jupiter masses) over a time span of typically 50 orbital periods. The initial velocity is pure Keplerian rotation ($u_r = 0, u_\varphi = \Omega_K r = (GM_*/r)^{1/2}$), and the temperature stratification is always given by $T(r) \propto r^{-1}$ which follows from an assumed constant vertical height H/r . For these isothermal models the temperature profile is left unchanged at its initial state throughout the computations.

For our standard model we use a constant kinematic viscosity coefficient ν .

5.1.2 Initial Setup: 3D

For the 3-dimensional model we use the same setup as described in the previous section. The grid in the θ direction is either one of two possibilities: First for vertically symmetric initial conditions we use only the lower half of the disk: $\theta_{\min} = 90^\circ, \theta_{\max} = 105^\circ$, so we save half the computational time making use of the symmetry of the system. For vertically asymmetric initial conditions, when the initial inclination of the planet is non-zero, we use $\theta_{\min} = 75^\circ, \theta_{\max} = 105^\circ$. For the usual disk geometry factor $H/r = 0.05$ this means we have 5 scale heights of the disk in our computational domain.

The density profile in the θ -direction is Gaussian with a scale height given

by H . Although this model is not exactly in equilibrium with the Keplerian velocity profile, it is close enough for our purposes.

5.2 EU Comparison project - a test case

There are many standard tests to check a hydrodynamical code but none of them come close to the type of problems we would like to solve. To make sure the code works correctly for the problem of a protoplanetary disk with an embedded planet, we participated in the EU Code Comparison project set up by Pawel Artymowicz and Miguel de Val Borro (Stockholm Observatory)^c. 17 different codes were compared on the problem of Jupiter and/or Neptune embedded in a protoplanetary disk, which resulted in a joint paper (de Val Borro *subm*). We will list the results and conclusions for our contribution here in more detail than in the paper.

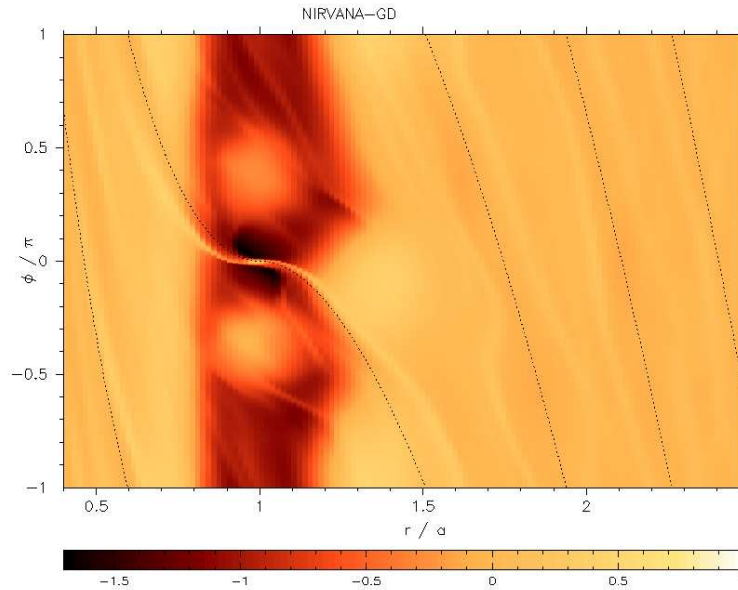


Figure 12: $r - \phi$ plot of the surface density after 100 orbits of the planet for the model with a planet mass of $q = 10^{-3}$ and no viscosity (Model JI).

We have calculated the standard models Jupiter Inviscid (JI), Jupiter Viscous (JV), Neptune Inviscid (NI) and Neptune Viscous (NV) with different resolutions, the standard resolution of 128×384 cells, and higher resolutions

^c<http://www.astro.su.se/groups/planets/comparison/>

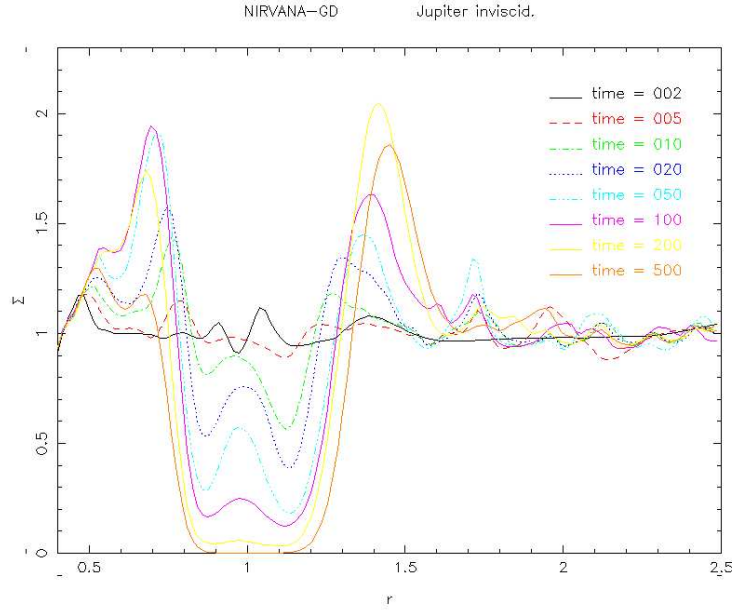


Figure 13: The azimuthally averaged radial surface density profile at several times (in orbits of the planet) for the model with a planet mass of $q = 10^{-3}$ and no viscosity (Model JJ). The dotted lines in the plot show the theoretical location of the spiral waves for a low-mass planet. The deviation from this is clear for this high-mass planet.

for the viscous Jupiter case (models JV*a*, JV*b*). The suffix 'a' denotes a two times higher resolution (256 x 768), and the suffix 'b' for a four times higher resolution (512 x 1536). We found that our results compare very well to those of the other grid-based methods, although we have the impression that some participants have used a different prescription for the damping radial boundary conditions described in 4.5.2 as the amount of wave reflection at the outer boundary was higher in our code. We also investigated if the initial resolution was sufficient for the set problem to get accurate results: would higher resolution calculations look the same as the lower resolution ones? This question is discussed in section 5.2.4.

5.2.1 Initial conditions

The initial conditions were used as described above, except for the time scale on which the mass of the planet is turned on. This was taken as 5 orbital periods for both the $q = 10^{-3}$ model (Jupiter) and the $q = 10^{-4}$ model (Neptune).

5.2.2 Jupiter inviscid

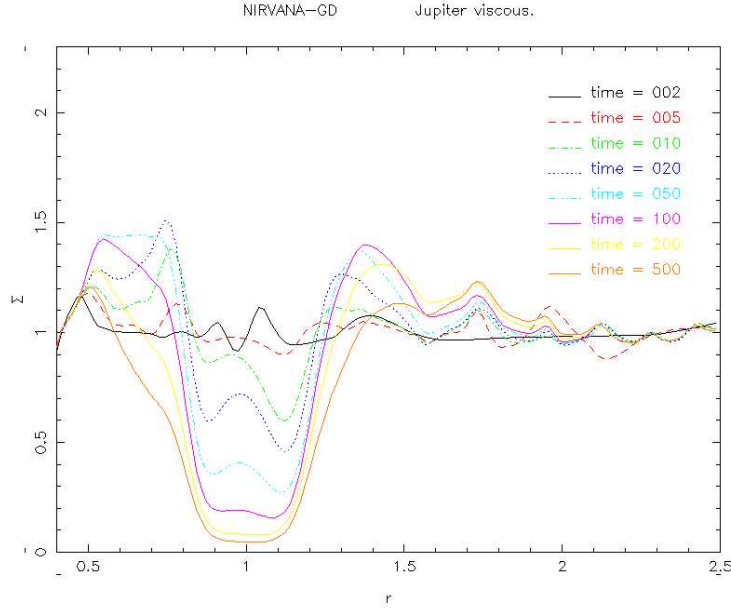


Figure 14: The azimuthally averaged radial surface density profile at several times (in orbits of the planet) for the model with a planet mass of $q = 10^{-3}$ and a dimensionless physical viscosity of $\nu = 10^{-5}$ (Model JV).

In NIRVANA we turned off the viscosity routine completely for this run so we are left with only the numerical viscosity caused internally by the algorithm. The planet quickly opens a gap that becomes very clean and very deep, however at the Lagrangian points L4 and L5 there is a large amount of matter left. This will travel on librating and horseshoe orbits and will stay there for a long time in these calculations.

One can clearly see the spiral shocks caused by the planet in Figure 12. These spiral arms are not exactly where they should be according to the linear approximation but this is caused by the already quite large planet mass.

We also observe the formation of vortices on both sides of the gap. The large density gradients at the edge of the gap cause instabilities, and these will not be damped by the viscosity. The vortices move with local Keplerian speed and will therefore move around quickly in the co-rotating frame. In long term evolution, the influence on the torque on the planet will be averaged out.

The gap in this case is very deep and clean as can be observed in the a-

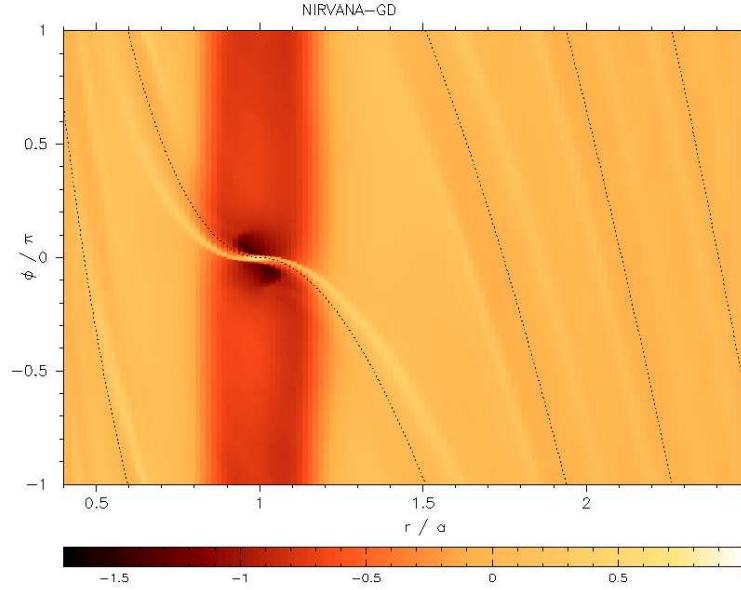


Figure 15: $r - \varphi$ plot of the surface density after 100 orbits of the planet for the model with a planet mass of $q = 10^{-3}$ and a numerical dimensionless viscosity of $\nu = 10^{-5}$ (Model JV). As can be seen from the relative position of the spiral waves with respect to the theoretical location for a low-mass planet, viscosity does not change the position of the spiral waves.

azimuthally averaged surface density plot in Fig. 13. The dotted lines in the plot show the theoretical location of the spiral waves in linear theory, i.e. when the planet mass considered a small number. For Neptune ($q = 10^{-4}$) this assumption is reasonable as can be seen in Fig. 13, for Jupiter this assumption is no longer valid: we are in the non-linear regime.

5.2.3 Jupiter viscous

With the physical viscosity set at $\nu = 10^{-5}$ the flow is much smoother than in the inviscid case. The gap opened by the planet is narrower than in the inviscid case as can be seen in the azimuthally averaged surface density plot in Figure 14. As the widening of the gap by the planet is counteracted by the closing of the gap by the viscosity.

If we look at the surface density plot after 100 orbits (see Figure 15) we notice that the material at the Lagrangian points disappears much more quickly. Finally we do not see vortices at the gap edges that were present in the inviscid case. Any instabilities that would form are sufficiently damped away by the

viscosity.

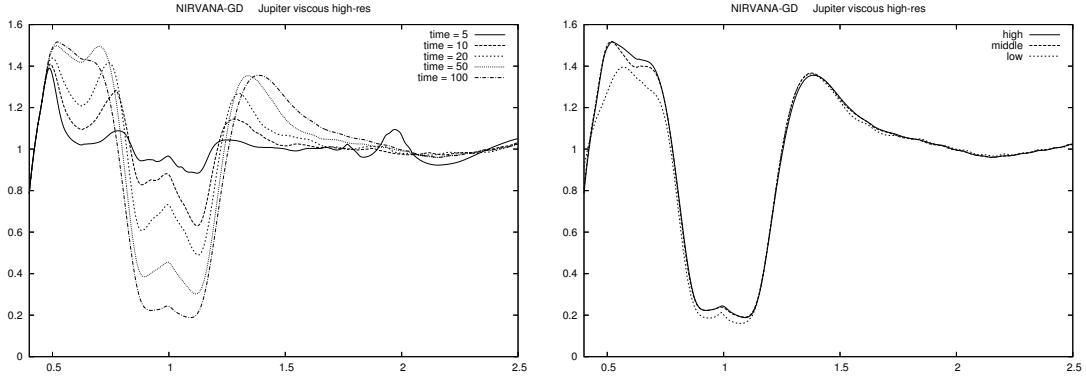


Figure 16: A resolution study of model JV. **left**) The azimuthally averaged radial surface density profile at several times (in orbits of the planet) for the model as in Fig. 14 but with a four times higher resolution of $N_r = 512$, $N_\phi = 1536$ (Model JVb). **right**) The azimuthally averaged surface density after 100 orbits. The low resolution is the standard resolution where $N_r = 128$ and $N_\phi = 384$ (Model JV). The middle resolution is 256×768 cells (Model JVa), the high resolution is 512×1536 cells (Model JVb).

5.2.4 High resolution

In this standard case we have also performed a resolution study to see if the resolution of the standard model is sufficient to solve the problem at hand. For this we ran the model at a two times higher resolution (Model JVa) and a four times higher resolution (Model JVb). The latter model took 10 days on a single processor machine, as could be expected since the computational time will scale with the resolution to the third power (In a 2-dimensional calculation, the number of grid cells will scale with the square of the resolution, and the time step will scale with the inverse of the resolution, so to complete one orbit the required CPU time scales with the cube of the resolution).

In the left graph of Fig. 16 the azimuthally averaged density profile at different times is shown for the highest resolution calculation (Model JVb). It can clearly be seen that the evolution is similar to that of the low-resolution case (Model JV). To compare the final result of both calculations, in the right graph of Fig. 16 the azimuthally averaged density profile after 100 orbits is shown for the three different resolutions. There is a slight difference in the gap depth: For the lowest resolution the gap is slightly deeper. More significantly different is

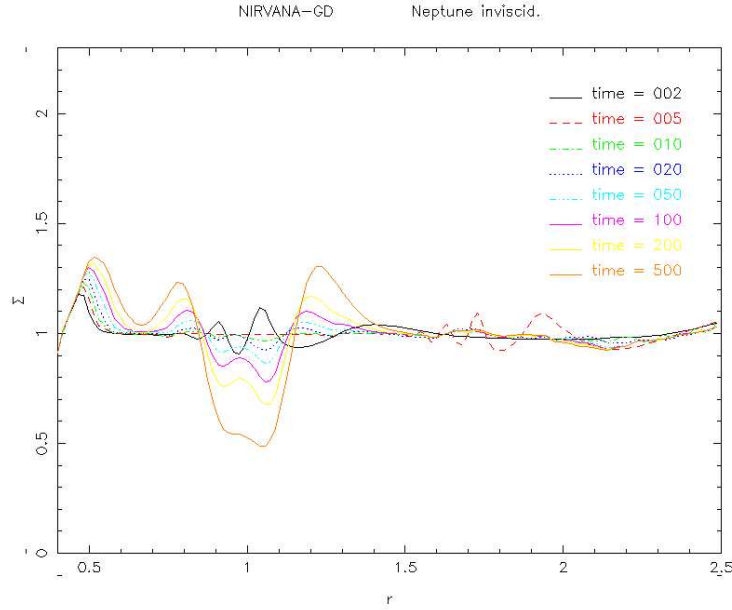


Figure 17: The azimuthally averaged radial surface density profile at several times (in orbits of the planet) for the model with a planet mass of $q = 10^{-4}$ and no viscosity (Model NI).

the density bulge in the inner disk: this is different and has still not converged for the highest resolution. This can be explained by the use of the uniform grid in r : The relative resolution near the inner boundary and the high density gradients by the tightly wound spirals in this region make the required resolution very high and the effective resolution relatively low. However, this part of the disk is not essential for calculating the migration and accretion properties of the planet. As such we can say that it is reasonable to take the lowest resolution model.

5.2.5 Neptune inviscid

For a ten times lower planet mass of $q = 10^{-4}$ the gap will not be completely cleared out. The depth of the gap as a function of time is shown in Figure 17. Also the spiral arms are significantly weaker than in the Jupiter case and follow the theoretical path predicted by linear analysis much more closely, see Figure 18. de Val Borro (subm) report vortices in this case around the gap edges, although much smaller and less prominent than in the Jupiter case. In our simulations we find no evidence of vortices for this planetary mass.

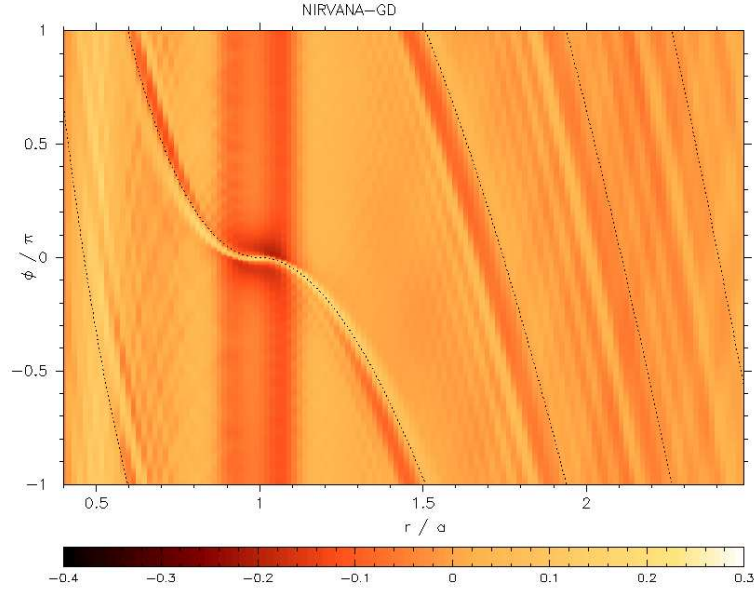


Figure 18: $r - \phi$ plot of the surface density after 100 orbits of the planet for the model with a planet mass of $q = 10^{-4}$ and no viscosity (Model NI). Here the dotted lines denoting the theoretical position of the spiral waves for a low-mass planet are followed much closer than for the Jupiter case.

5.2.6 Neptune viscous

In comparison with the inviscid case the flow is much smoother here, and there are no vortices. The surface density after 100 orbits is shown in the bottom graph of Fig. 19. Although there is a gap, the planet is still partially embedded in the disk. The depth of the gap as a function of time can be readily viewed in the radial surface density plot in the top graph of Fig. 19.

5.2.7 Conclusions

From the calculations performed in this test case it is apparent that for the actual problem the initial resolution is sufficient, however for local effects like accretion onto the planet a higher resolution may be preferable. Our version of NIRVANA agrees well with other similar methods, and although we cannot be sure of the definitive answer, the resolution study shows that we have come close enough to set a bench mark for future programmers to test their methods on this problem.

Also, as there is a slight difference between the radial surface density pro-

file for the low resolution study JV and the two higher resolution models JVa and JVb, we suggest performing the test on the middle resolution. With the currently available computing power this should be no problem for anyone wanting to benchmark his program with the comparison project. The complete data of the comparison project can be found on Miguel de Val Borro's website^d and the comparison paper (de Val Borro *subm*).

^d<http://www.astro.su.se/miguel/comparison/>

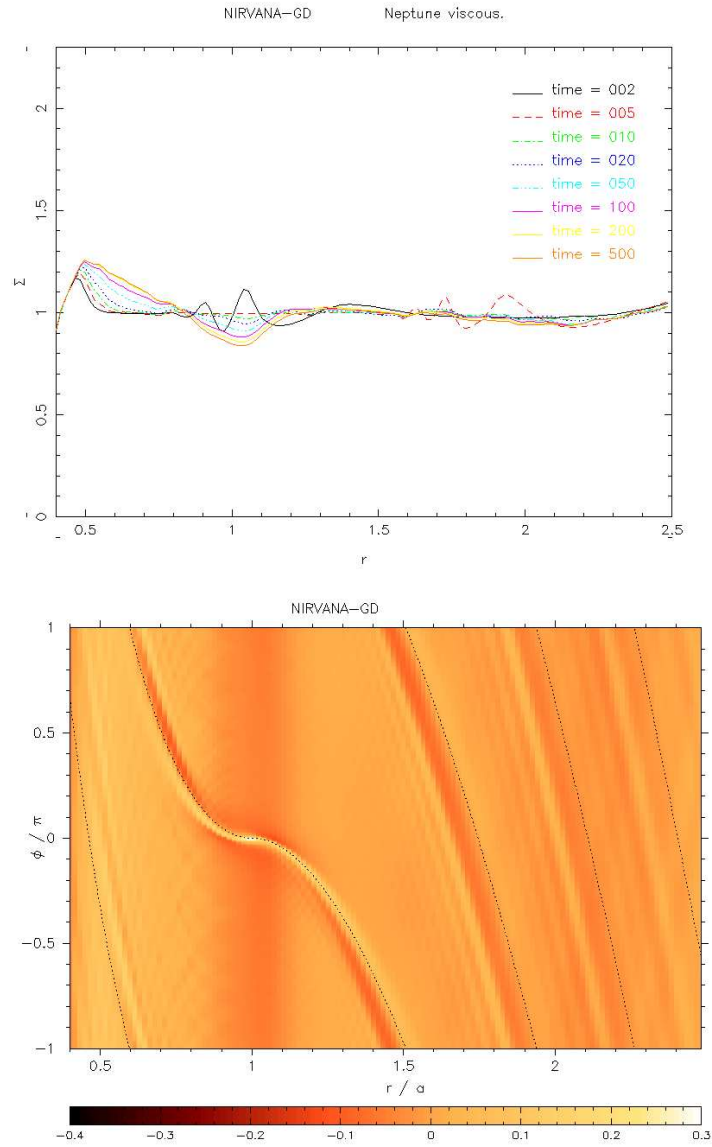


Figure 19: **top**) Radial surface density profile at several times (in orbits of the planet) for the model with a planet mass of $q = 10^{-4}$ and a numerical dimensionless viscosity of $\nu = 10^{-5}$, **bottom**) $r - \varphi$ plot of the surface density profile after 100 orbits of the planet for the model with a planet mass of $q = 10^{-4}$ and a numerical dimensionless viscosity of $\nu = 10^{-5}$ (Model NV).

6 Eccentricity excitation in disks

The most exciting phrase to hear in science, the one that heralds new discoveries, is not 'Eureka!' (I found it!) but 'That's funny ...'

- Isaac Asimov

As discussed in section 3.5 there are still several problems to be solved in the area of disk-planet interaction, one of which is the problem that very massive planets need to form on a timescale that is shorter than the life time of the disk. This chapter discusses a state in which the accretion rate onto a planet with a much higher mass relative to the host star than Jupiter can be enhanced. Jupiter has a mass ratio to the Sun of almost exactly 10^{-3} . However, some planets have been found with over 5 Jupiter masses around solar type stars. Similarly some red dwarf stars have Jupiter-like companions. In our dimensionless calculations these planets are treated in the same way. The results in this chapter have also been published in Kley and Dirksen (2006).

In the core accretion theory described in section 3.1 there are several problems for making these very massive planets. As soon as the planet opens a gap in the disk (when it reaches a mass of several tenths of a Jupiter mass) accretion slows down but is not stopped, but after the planet mass reaches several Jupiter masses, an order of magnitude more, the gap is much larger already and accretion slows down to a rate where building planets of 5 – 10 Jupiter masses is no longer feasible in the life time of a disk, which is about 10^7 years.

6.1 Large planet simulations

One of the most well-known multiple-planet systems is Gliese 876, where two gas giants orbit in a 2:1 resonance with orbital periods of 60 and 30 days (Marcy et al. 2001). The planets in the system also have a very high planet mass to star mass ratio, the heaviest planet having a mass ratio of 0.0059 to the star. Only the low total mass of the system (the central star is an M dwarf) and the resonant orbital periods of both planets make the system gravitationally stable. When a model of the system was run for several thousand orbits (Kley et al. 2005) a new periodic state for the disk was found and here we investigate

this periodic state in more detail.

6.2 The dual-state disk

We first consider our standard model as described in chapter 4 using a planetary mass ranging from 1 to $5 M_{Jup}$, i.e. a mass ratio of $q = 10^{-3}$ to $5 \cdot 10^{-3}$. The other physical parameters are identical to the models described in section 5.1.1. Due to the nature of the damped boundary conditions and a non-zero physical viscosity of $\nu = 10^{-5}$ we might expect, after a sufficiently long evolution time, a convergence towards an equilibrium state where the density structure and the total amount of mass inside the computational domain remain constant in time, at least in the co-rotating frame as in the $1 M_{Jup}$ case described in chapter 5.2. Indeed, for smaller planetary masses of $M_p < 3M_{Jup}$ we find such a circular stationary state which displays the typical features of embedded planets in disks: a deep, circular depression of density at the location of the planet (the gap), spiral arms in the inner and outer disk. This state is shown in the left graph of Fig. 20, which shows the surface density of the obtained equilibrium state at an evolutionary time of $t = 2000$ orbits.

However, if the planetary mass is larger, $M_p \geq 3M_{Jup}$ the system surprisingly does not reach a stationary equilibrium state anymore. Instead we find after a very long time (> 1000 orbits) a new periodic state which has approximately the same period as the orbital period of the planet. In this state the disk is clearly eccentric with an extremely slow precession rate such that the eccentric pattern appears to be nearly stationary in the inertial frame. This eccentric quasi-equilibrium state for $M_p = 5M_{Jup}$ is shown in the right graph of Fig. 20.

6.3 The eccentric disk

To look at this second equilibrium state in more detail, we define a measure of the eccentricity of the disk that is calculated as follows: For a ring at radius r_i we calculate the eccentricity for every cell in the ring from the velocity and position vector of that cell by assuming the fluid element is a particle moving freely in the central potential of the star, feeling no pressure forces, i.e. the eccentricity a test particle on a Keplerian orbit at the location of the fluid

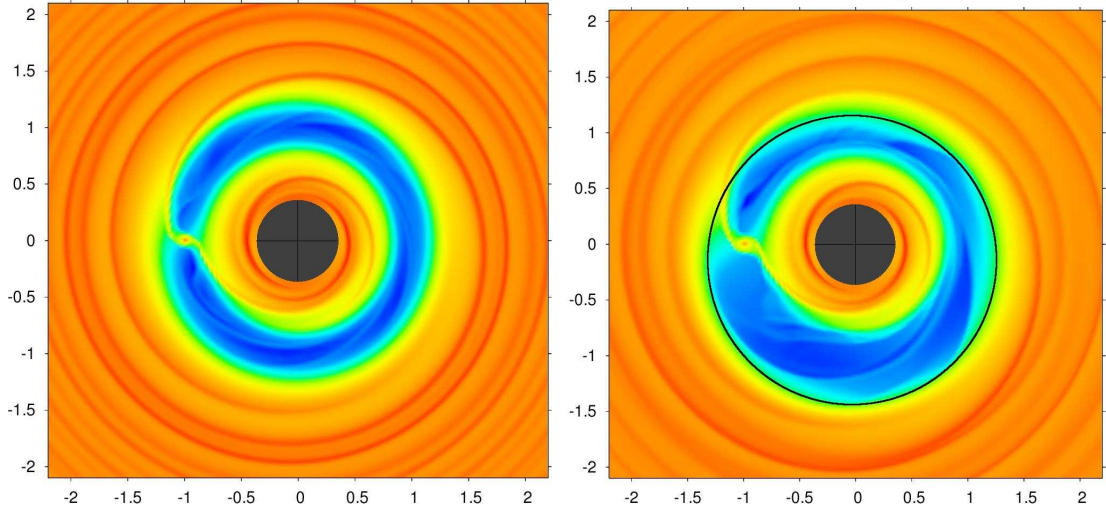


Figure 20: Logarithmic plots of the surface density Σ for the relaxed state after 2000 orbits for two different masses of the planet which is located at $r = 1.0$ in dimensionless units. **Left)** $q = 3.0 \cdot 10^{-3}$ and **Right)** $q = 5.0 \cdot 10^{-3}$ calculated with NIRVANA. The inner disk stays circular in both cases but the outer disk only in the lower mass case. For $q = 5.0 \cdot 10^{-3}$ it becomes clearly eccentric with some visible fine structure in the gap. For illustration, the drawn ellipse (solid line in the lower plot) has one focus at the stellar location and an eccentricity of 0.20.

element. The average eccentricity over all cells in the ring is then defined as the eccentricity of the disk at that radius r_i . This value is plotted for different masses in Fig. 21 at the evolutionary time of $t = 2500$, only for $M_p = 3M_{Jup}$ at $t = 3850$ orbits.

For planetary masses below around $M_p \approx 3M_{Jup}$, the maximum eccentricity of the disk is about 0.10, and is strongly peaked at $r \approx 1.2$. For the larger planetary masses the eccentricity of the disk nearly doubles and reaches 0.22 for $M_p = 5M_{Jup}$. In addition, a much larger region of the disk has become eccentric, which has been seen clearly already in the surface density distribution in the right graph of Fig. 20, where an ellipse is drawn with an eccentricity of 0.20 and one focus at the position of the central star. This ellipse follows the outer edge of the gap with a high degree of accuracy. Although the gap edge is almost stationary in the rotating frame, we find a small and typically prograde precession rate $\dot{\varpi}$ for the eccentric disk. From our longest runs (over several thousand orbits) we estimate $\dot{\varpi} \approx 10^\circ/1000$ orbits. In Fig. 21 the curves for the lower planet masses end at $r = 2.5$ because this is the outer boundary for

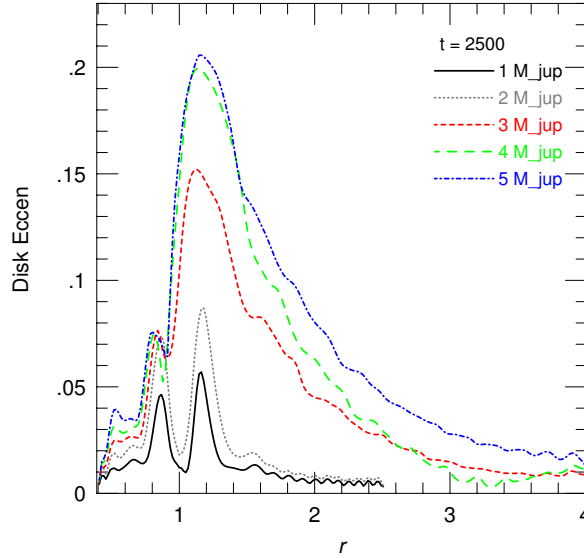


Figure 21: Disk eccentricity as a function of radius for the several models with $q = 0.001$ up to $q = 0.005$ at $t = 2500$ orbits, for the $q = 0.003$ model at $t = 3850$. For the two lower curves $q = 0.001$ and $q = 0.002$, the outer edge of the computational domain lies at $r_{max} = 2.5$.

those low mass models.

In Fig. 22 the azimuthally averaged density profile is plotted for different planetary masses for the same models as in Fig. 21. Clearly the gap width increases for the larger planet mass, as expected due to the stronger gravitational torques. For the lowest mass ($q = 0.001$) model (solid line) the gap is not completely cleared. Observe that the slope of the outer gap edge for the models with 4 and 5 Jupiter masses in the range $1.1 < r < 1.3$ is shallower than for the other models. This is evidence of the eccentric disk.

6.4 Dependencies on numerical parameters

As will become clear in section 6.6 there is a threshold mass above which the disk will become eccentric. It is intimately connected to the shape, depth and width of the gap, and parameters that will change the gap structure will also change this threshold mass. Before we analyze physical influences we display in Fig. 23 the surface density profile and the disk eccentricity for models using different numerical parameters but all with same physical setup for $q = 0.004$, and at the same evolutionary time of 2500 orbits (the high resolution model at

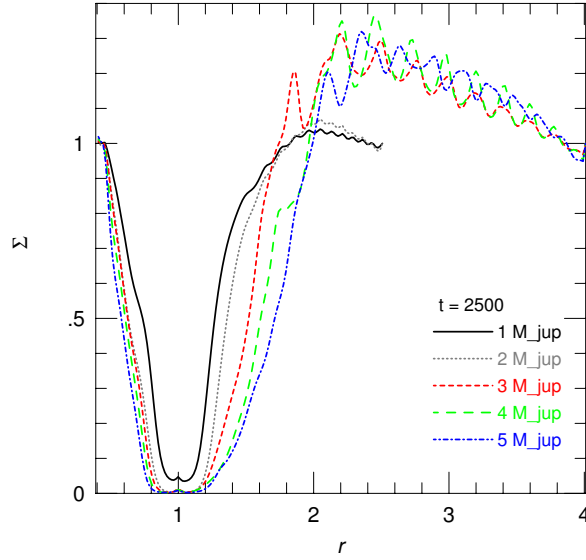


Figure 22: Azimuthally averaged radial profiles of the surface density for different planet masses, for the same models and times as in Fig. 21. The width of the gap increases with planetary mass.

$t = 1750$ orbits).

The solid line refers to the basic reference model (as in Fig. 22, $4M_{Jup}$ model). We first find that the mass value where the transition occurs may depend on the location of the outer boundary r_{max} . If the stand-off distance of the planet to the outer boundary is too small the damping boundary conditions, which tend to circularize the disk, prevent the disk from becoming eccentric. The simulations using a $4M_{Jup}$ planet and a smaller r_{max} clearly shows this effect. For this mass of the planet the disk will not anymore become eccentric for $r_{max} = 2.5$ (dotted curve). Hence, to properly study this effect a sufficiently large r_{max} has to be chosen. An extended domain with $r_{max} = 10$ instead of $r_{max} = 4$ (short-dashed-dotted line) does not alter the eccentricity behavior of the disk. From this we conclude that $r_{max} = 4$ is sufficient for our calculations. The inner disk remains circular for all planet masses because of the strong damping introduced by the boundary condition.

A higher resolution (200×500 , short-dashed line), and running the model in the inertial frame (long-dashed) have no significant influence on the density distribution and the occurrence and magnitude of the disk eccentricity. A lower resolution model (long-dashed-dotted) using 128×128 grid cells, results in a

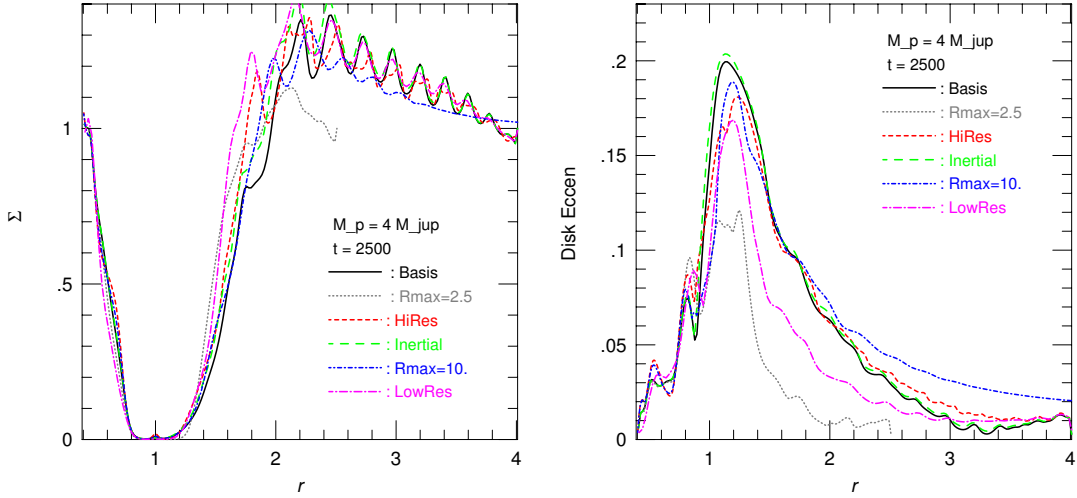


Figure 23: Surface density and eccentricity profile for models using $q = 0.004$ at a time of 2500 orbits, the high resolution (model short dashed line) at 1750 orbits. Plotted are results for different models varying the numerical setup.

slightly lower eccentricity due to a larger (numerical) damping. In addition, we have compared the NIRVANA results with those for a different numerical code, RH2D (Kley 1989, see) and again found good agreement. Hence, we conclude that the eccentric disk state is a robust, reproducible physical phenomenon.

6.5 Dependencies on physical parameters

In Fig. 24 we display the surface density profile and the disk eccentricity for models with $q = 0.004$ using different physical parameters. If the dimensionless viscosity ν is enlarged to 3×10^{-5} (dotted line) the gap width and depth is reduced and the disk will no longer become eccentric for the planet mass of $q = 0.004$ (and also not for $q = 0.005$). Similarly, an increased H/r (long-dashed line) leads also to a narrower gap and a smaller disk eccentricity. If, on the other hand, the viscosity is lowered by a factor of three (short-dashed), or H/r is reduced we find that the disk reaches about the same eccentricity as before.

The last model (dashed-dotted line) refers to a planet on an eccentric orbit with $e_p = 0.05$ and a 3 times higher viscosity than the basis model. As can be seen, the disk remains circular for these parameters. This model demonstrates

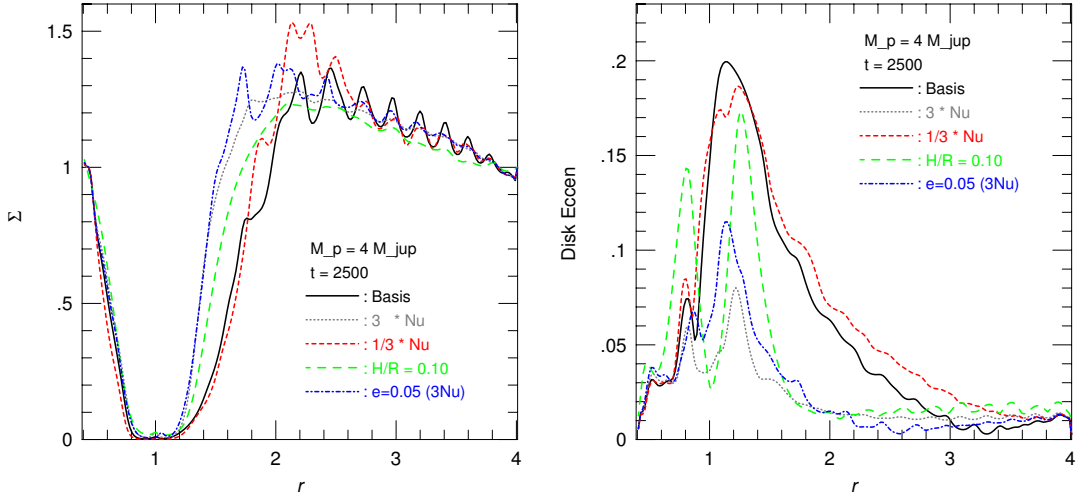


Figure 24: Surface density and eccentricity profile for models using $q = 0.004$ at a time of 2500 orbits. Plotted are results for different models varying the physical setup.

that it is not the planetary eccentricity which is responsible for producing the disk eccentricity but that it is rather a genuine instability. This conclusion is confirmed by a model with $M_p = 2M_{Jup}$ and $e_p = 0.05$ which (for the standard viscosity) does not produce an eccentric disk.

6.6 The two equilibrium states

To illustrate the effect under different physical conditions we present additional simulations using a slightly different setup. Here, we consider a planet moving inside a disk at a radius of 0.35 AU, assuming that the inner disk has been cleared already. The outer radius of the computational domain lies at 1.2 AU, and the inner one at 0.25 AU. The scale height of the disk is $H/r = 0.05$, and for the viscosity we use here as an alternative an α -prescription, with a constant value of $\alpha = 0.01$. In these models we have used a planetary eccentricity of $e_p = 0.01$ which is typically found in models of embedded planets that follow the orbital evolution. As shown above this value of e_p has no influence on the transition to the eccentric disk state. The remaining setup is similar to the models described above. The viscosity may be on the large side of protoplanetary disks but has (in combination with the lack of the inner disk) the clear advantage of speeding up the simulations considerably which allows us

to reach the quasi-equilibrium states in which global quantities such as mass, energy do not vary in time anymore, with reasonable computational effort. This alternative setup has been used recently in a paper modeling the resonant system GJ 876 and it is described in more detail in Kley et al. (2005). Here we describe additional results concerning details of the eccentric disk state.

For these α -models we vary the planet-star mass ratio q from $1 \cdot 10^{-3}$ to about $7 \cdot 10^{-3}$. In all cases the models are evolved until a quasi-stationary state has been reached. As already seen above for the constant viscosity case, also in this case the disk changes its structure from circular for small planetary masses to eccentric for large planetary masses. Here the transition occurs at a larger planetary mass because of the higher effective viscosity.

In Fig. 25 we display the mass accretion rate onto the planet as a function of the planet mass. There is a strong jump in the magnitude of the accretion rate at a critical planetary mass $q_{crit} \approx 5.25 \cdot 10^{-3}$, exactly at the point where the disk switches from circular to eccentric. For small planetary masses $q < q_{crit}$ the mass accretion rate falls off with increasing planetary mass, because upon increasing M_p the stronger gravitational torques will deepen the gap and reduce the accretion rate (Bryden et al. 1999; Lubow et al. 1999). However, when the disk turns eccentric the gap edge periodically approaches the planet and it may even become engulfed in the disk material for sufficiently large eccentricity (see Fig. 26). Consequently, the mass accretion rate onto the planet is strongly increased allowing for more massive planets.

This sudden change in the accretion rate is reminiscent of a *phase transition* where the ordering parameter is given here by the planetary mass. Test simulations have shown that the obtained equilibrium structure does not depend on the initial configuration (e.g.. density profile, initial mass in the disk) but is solely given by the chosen physical parameters. As shown above the transition from the non-eccentric state to the eccentric state, which is here a function of only the planetary mass, depends also on the viscosity and temperature on the disk which we have held fixed in this model sequence.

Similarly to accretion rate the total disk mass contained in the system also changes abruptly at the q_{crit} as a consequence of the applied the boundary conditions at r_{max} . These are chosen such that the disk relaxes towards its

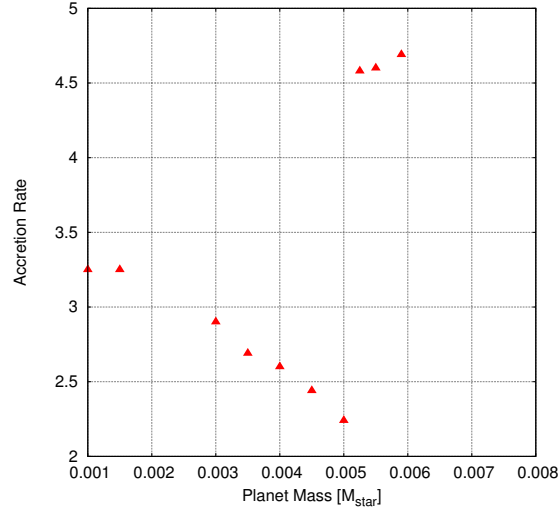


Figure 25: The dependence of the accretions rate onto the planet (in dimensionless units) on the planetary mass for relaxed quasi-equilibrium configurations. Results are displayed for models using an $\alpha = 0.01$ viscosity.

initial conditions at the outer boundary, e.g. the value of the surface density is fixed at that point. Upon increasing the planet mass the gap becomes more pronounced and disk mass is pushed towards the outer boundary increasing the density there. At the onset of the eccentric state this relation changes abruptly.

The existence of the two equilibrium states of the disk is further illustrated in Fig. 26 where we display gray scale plots of the surface density Σ for the relaxed state. for two different mass ratios ($q = 4.5$ and $5.9 \cdot 10^{-3}$) in a $r - \varphi$ representation. While for the lower mass case ($q = 4.5 \cdot 10^{-3}$) the disk structure remains quite regular (left panel), the second high mass case ($q = 5.9 \cdot 10^{-3}$) shows a strongly disturbed disk which has gained significant eccentricity ($e = 0.2$) where also the gap edge becomes highly deformed (right panel, also compare to Fig. 20).

6.7 Eccentricity growth rates

The growth of the eccentricity of the disk depends primarily on the mass of the planet. To measure the speed of the increase we analyze the time dependence of the total radial kinetic energy $E_{kin,rad}$ in the models, because this is a quantity most readily available. In the top panel of Fig. 27 we display the $E_{kin,rad}(t)$

for four different planet masses. For a low mass of $M_p = 2M_{Jup}$ no growth is visible but for larger planets the growth time shortens upon increasing M_p . From the growth of $E_{kin,rad}(t)$ we estimate visually the growth-times τ as a function of planetary mass (lower panel of Fig. 27). Clearly, for more massive planets the disk will turn eccentric much faster. From the plot we may estimate a growth rate $\gamma = 1/\tau \propto M_p^{2.4}$, a relation which is indicated by the additional straight line in the graph. This dependence on planetary mass is somewhat stronger than that estimated on theoretical grounds (Papaloizou et al. 2001).

6.8 Analysis of one orbit of the eccentric disk

After several thousand orbits in the eccentric state, the disk settles down to a situation where the elliptic shape of the gap is exactly preserved at the same position in space. Since we are in the co-rotating frame, this means that the complete picture with planet and disk is periodic with a period of one orbital period of the planet.

In the slides shown in Fig. 28 the eccentric disk at different phases of the planet orbit are shown. The shape of the gap is very stable, but every time the planet passes near the material that represents the periastron of the outer edge of the gap there is a wave going down the outer Lindblad spiral into the planet Roche lobe as can be seen in the top left panel. At the same time much of the outer Roche lobe spiral will get embedded into the outer disk. The density enhancement of approximately a factor two is then accreted onto the planet. In the top right panel it the density around the planet is enhanced, and in the bottom left panel the matter around the planet is being accreted. Here the planet is near the widest part of the gap. Finally in the bottom right panel one can see the planet in the normal state for a non-eccentric disk. All the material around it has been accreted or dispersed, however the planet is already approaching the narrow part of the gap again. This mechanism is the main source of the increased accretion rate.

Before a stable periodic state with a period of exactly 1 orbital period of the planet is reached after several thousand orbits, first an intermediate stage is present where the disk precesses. This precession rate then decreases with time until no more precession is present. At this point, the pure periodic state

is reached and this can be kept running in the simulation for an arbitrary long time (the longest simulation was 5000 orbits, of which 2000 orbits without precession).

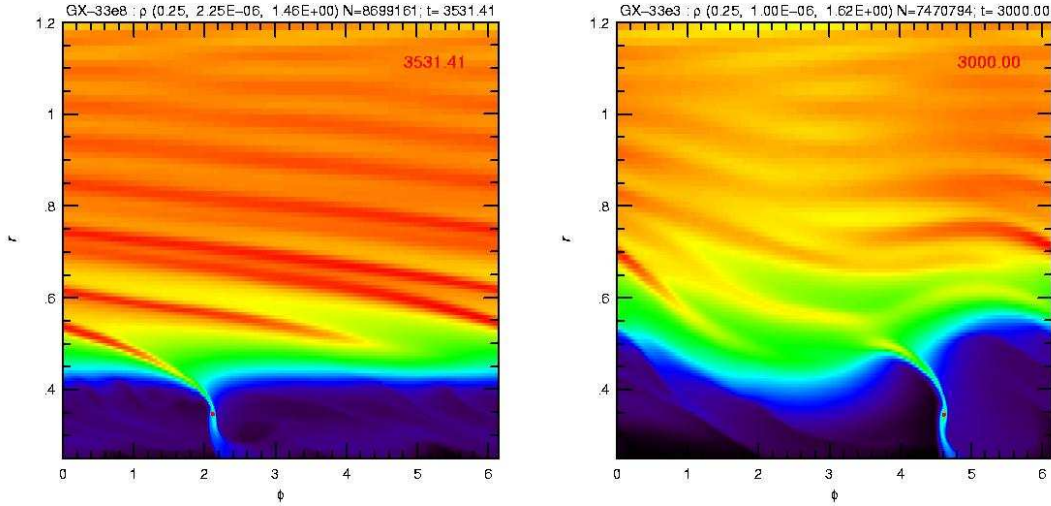


Figure 26: Gray scale plots of the surface density Σ for the relaxed state for two different planetary masses: **a)** $q = 4.5 \cdot 10^{-3}$ and **b)** $q = 5.9 \cdot 10^{-3}$ calculated with RH2D. Due to the higher planetary mass much stronger wave-like disturbances are created in the density.

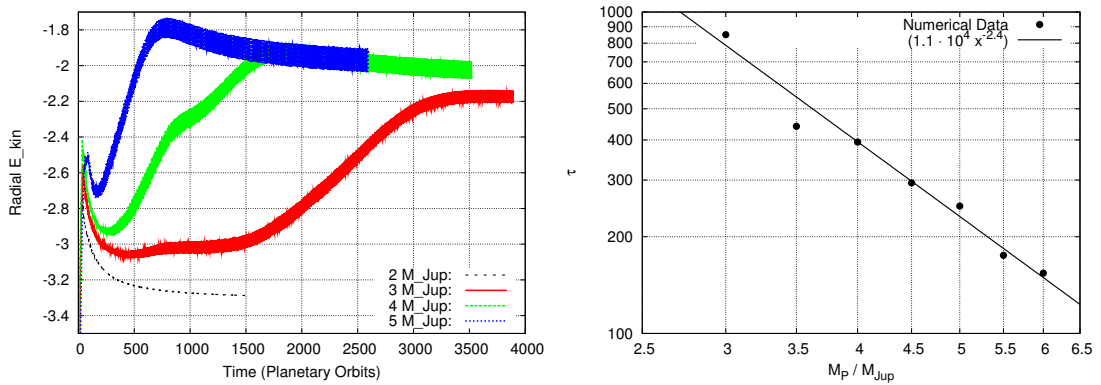


Figure 27: **left)** The time dependence of the total radial kinetic energy of the disk in the computational domain for four different planet masses. **right)** the growth rate of the eccentric disk mode as a function of the planetary mass. The superimposed straight line has a slope of $\tau \propto M_p^{-2.4}$.

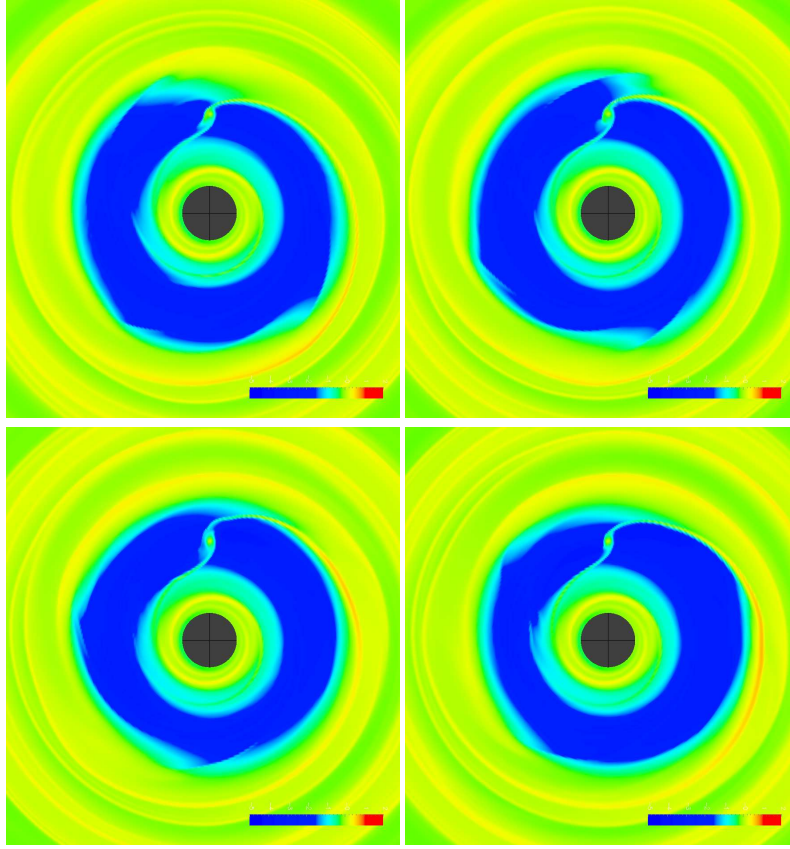


Figure 28: Snap shots of a planet in an eccentric disk. As can be seen the planet moves from the wide part of the gap into the narrow part and back. When it gets to the narrowest part the accretion rate will increase dramatically.

6.9 Theoretical analysis

The observed growth of the disk eccentricity in our simulations resembles that found by Papaloizou et al. (2001) for very massive planets with $M_p \gtrsim 10M_{Jup}$. The effect can be explained by a tidally driven eccentricity through resonant interaction of the disk with particular components of the planet's gravitational potential (Lubow 1991a).

Using cylindrical coordinates (r, φ) we decompose the planetary potential Φ_p into its different Fourier components and write

$$\Phi_p(r, \varphi) = \sum_{m=0}^{m=\infty} \Phi_m(r) \cos[m(\varphi - \Omega_p t)] \quad (6.1)$$

where Ω_p is the angular frequency of the planet. Here the planet is on a *circular*

orbit. The response of the disk has the form

$$\propto \exp[i(k\varphi - l\Omega_p t)]$$

with k and l integer values.

The planetary potential produces tides in the disk which interact with an initially small eccentric disk. The m -th Fourier component of the potential ($\Phi_m(r)$ in Eq. 6.1) excites an eccentric Lindblad resonance in the *outer disk* where the rotation period of the disk is $\Omega = \frac{m}{m+2}\Omega_p$ which corresponds to the mode $(k, l) = (m + 1, m)$ (Lubow 1991a). Hence, for an eccentric ($m = 1$) perturbation the radial location lies at the outer 1:3 resonance at $r \approx 2.08$. As the mass of the planetary companion increases, the gap it opens in the disk will be deeper and wider. Already in Artymowicz (1992) it was suggested that for sufficiently wide gaps, eccentricity growth can be induced by interaction at the 1:3 resonance in the outer disk, However, for smaller planet masses this is damped by other resonances which are listed in Goldreich and Sari (2003); Sari and Goldreich (2004). The main contributing eccentricity-damping resonances are the co-orbital resonances and the resonances located at the outer 1:2 resonance. Only if the gap is deep and wide enough these two resonances can no longer cancel the eccentricity-exciting effect of the interaction at the 1:3 resonance. The radial surface density profiles for simulations with different planet masses at 2500 orbits have been displayed in Fig. 22. As can be seen, only for planet masses larger than approximately $3 M_{Jup}$ the gap is sufficiently cleared at the 1:2 resonance ($r \approx 1.58$) to allow for an eccentricity increase of the disk. In the next section we derive the existence and properties of these resonances.

6.10 Disk modes

Assume a flat disk subject to a point mass potential $\Phi_0(r)$ and a component of the planet's potential of the form $\Phi_m(r, \theta, t) = \Phi_m(r) \cos[m(\theta - \Omega_p t)]$. The disk consists of isothermal gas and has surface density σ and sound speed c_s , so the specific enthalpy is $h(\sigma) = c_s^2 \log(\sigma)$.

The fluid equations in cylindrical coordinates (r, φ) for such a disk are (Lubow 1991a):

$$\begin{aligned} \frac{\partial \sigma}{\partial t} + \frac{\partial r \sigma u}{r \partial r} + \frac{1}{r} \frac{\partial \sigma v}{\partial \varphi} &= 0 \\ \frac{\partial u}{\partial t} + u \frac{\partial u}{\partial r} + \frac{v}{r} \frac{\partial u}{\partial \varphi} - \frac{v^2}{r} &= -\frac{\partial \Phi}{\partial r} - \frac{\partial h}{\partial r} \\ \frac{\partial v}{\partial t} + u \frac{\partial v}{\partial r} + \frac{v}{r} \frac{\partial v}{\partial \varphi} + \frac{uv}{r} &= -\frac{1}{r} \frac{\partial \Phi}{\partial \varphi} - \frac{1}{r} \frac{\partial h}{\partial \varphi} \end{aligned}$$

Here (u, v) are the velocities in radial and azimuthal direction, respectively.

The equilibrium state for such a disk, including full tidal effects of the external potential Φ , will be denoted by capital letters, so it is given by density Σ , radial velocity U , azimuthal velocity $V + \Omega(r)r$ and specific enthalpy H . We then write the external potential Φ as a Fourier series:

$$\Phi(r, \varphi, t) = \Phi_0(r) + \sum_{m=0}^{m=\infty} \Phi_m(r) \cos[m(\varphi - \Omega_p t)] \quad (6.2)$$

and expand all variables to the different components of the Fourier series. We write the equilibrium state for the different components of the potential for any quantity X as $X = X_0 + X_1 + \dots$

Now we consider a linear perturbation of the disk from its equilibrium solution which is caused by some initial eccentricity in the disk. Primes denote the linearly perturbed variables. We want to know if the eccentricity grows in the case of a finite perturbing potential in the limit of small eccentricity. For assuming linearity we require that e is small compared to $\Phi_m/(\Omega^2 r^2)$.

To solve the above equations we follow the notation in Lubow (1991a) and expand the perturbed variables in Fourier components of the perturbing potential Φ_m . Therefore we write any perturbation X' as $X' = X'_0 + X'_1 + \dots$, where the subscript denotes the component of the perturbing potential in the expansion.

6.10.1 Initial eccentric perturbation

To start with a seed for eccentricity growth we impose a small initial perturbation in the form of an eccentric disk, i.e. of the following form:

$$U'_0 = 2a(r) \sin(\varphi - \varpi) \quad (6.3)$$

$$V'_0 = a(r) \cos(\varphi - \varpi) \quad (6.4)$$

where ϖ is the angle of pericenter. We ignore precessional effects and regard ϖ as an arbitrary constant. $a(r)$ is an arbitrary but smooth function of r that is proportional to the local fluid eccentricity $e(r)$ as

$$a(r) = \frac{1}{2}\Omega r e(r). \quad (6.5)$$

As such $a(r)$ represents a small velocity perturbation that represents a small and azimuthally independent eccentricity field.

To zeroth order in Φ_m , the equilibrium state flow is axisymmetric:

$$\Sigma_0 = \Sigma_0(r), U_0 = V_0 = 0$$

and

$$H_0 = c^2 \log(\Sigma_0).$$

Substituting this equilibrium state into the linearized fluid equations, Lubow finds that to order Φ_m^0 in the perturbing potential the evolution equations for the eccentric perturbation are:

$$\frac{\partial U'_0}{\partial t} = +2\Omega V'_0 - \Omega \frac{\partial U'_0}{\partial \varphi} \quad (6.6)$$

$$\frac{\partial V'_0}{\partial t} = -\frac{1}{2}\Omega U'_0 - \Omega \frac{\partial V'_0}{\partial \varphi} \quad (6.7)$$

As these evolution equations also satisfy equations 6.3 and 6.4, we find no time-dependence of the eccentricity at this order.

6.10.2 To first order of the external potential

The next step is to include the next term of the planetary potential Φ_p . To first order of the external potential we find a new equilibrium flow that also gives rise to the Lindblad resonances. The equilibrium flow to first order in the external potential Φ_m of the unperturbed disk is well known, see for example Goldreich and Tremaine (1979):

$$U_1 = u_{nw}(r) \sin[m(\varphi - \Omega_p t)]$$

$$V_1 = v_{nw}(r) \cos[m(\varphi - \Omega_p t)]$$

where

$$u_{nw}(r) = \frac{1}{D_{nw}} \left[m(\Omega - \Omega_p) \frac{d\Phi_m(r)}{dr} + \frac{2m\Omega}{r} \Phi_m(r) \right]$$

$$v_{nw}(r) = \frac{1}{D_{nw}} \left[\frac{1}{2} \Omega(r) \frac{d\Phi_m(r)}{dr} + \frac{m^2}{r} (\Omega - \Omega_p) \Phi_m(r) \right]$$

and

$$D_{nw} = \Omega^2 - m^2(\Omega - \Omega_p)^2 \quad (6.8)$$

for $m > 0$. The subscript nw stands for non-wave as this equilibrium solution is time-independent in the frame co-rotating with the planet. As we will see, these first order terms will give rise to changes in the disk eccentricity.

To do so, we consider the linearly perturbed solution with the perturbation defined by equation 6.3, 6.4 to first order in the external potential and find two sets of equations for the velocities:

$$\frac{\partial U'_1}{\partial t} + \Omega \frac{\partial U'_1}{\partial \varphi} - 2\Omega V'_1 + \frac{\partial H'_1}{\partial r} = a(r)f(r) \cos[(m \pm 1)\varphi - m\Omega_p t + \varpi]$$

$$\frac{\partial V'_1}{\partial t} + \frac{1}{2}\Omega U'_1 + \Omega \frac{\partial V'_1}{\partial \varphi} + \frac{\partial H'_1}{r\partial \varphi} = a(r)g(r) \sin[(m \pm 1)\varphi - m\Omega_p t + \varpi]$$

where

$$f(r) = -\frac{1}{a} \frac{da u_{nw}}{dr} - \frac{m}{2r} u_{nw} \quad (6.9)$$

$$g(r) = \frac{dv_{nw}}{dr} + \frac{m+1}{2r} v_{nw} - \frac{1}{2ar} u_{nw} \frac{dar}{dr} \quad (6.10)$$

Propagating wave solutions to these equations are emitted from radii that satisfy the following resonance conditions. In case of a --sign:

$$\Omega = \frac{m}{m-2} \Omega_p, \Omega = \Omega_p \quad (6.11)$$

The former occurs for radii inside co-rotation with the planet, the latter coincides with co-rotation. This is called an eccentric inner Lindblad resonance.

In case of a +-sign:

$$\Omega = \frac{m}{m+2} \Omega_p, \Omega = \Omega_p \quad (6.12)$$

The former occurs for radii outside co-rotation with the planet, the latter coincides with co-rotation. This is called an eccentric outer Lindblad resonance.

For the rest of the analysis, we consider only the eccentric outer Lindblad resonances at $\Omega = m\Omega_p/(m+2)$.

For eccentric outer Lindblad resonances, the resonantly driven wave velocity response is of the form

$$U'_1(r, \varphi, t) = u_{w,s}(r) \sin[(m+1)\varphi - m\Omega_p t + \varpi] + u_{w,c}(r) \cos[(m+1)\varphi - m\Omega_p t + \varpi]$$

$$V'_1(r, \varphi, t) = v_{w,s}(r) \sin[(m+1)\varphi - m\Omega_p t + \varpi] + v_{w,c}(r) \cos[(m+1)\varphi - m\Omega_p t + \varpi]$$

The subscript w stands for wave, and subscripts s and c stand for sine and cosine components, respectively.

Eccentric corotational resonances can also be found in the above wave equations when combining the velocity equations with the mass conservation equation. Such resonances occur where

$$\Omega = m\Omega_p/(m \pm 1) \quad (6.13)$$

Goldreich and Tremaine (1981) demonstrated that these resonances can act to damp eccentricity. As can be seen easily, in the outer disk (+ sign in equation 6.13) there is an overlapping eccentric corotational resonance at the location of each eccentric Lindblad resonance except for the outer eccentric Lindblad resonance at $m = 1$, i.e. $\Omega = \frac{1}{3}\Omega_p$. To achieve global eccentricity growth the density profile in the disk must therefore be such that the $m = 1$ outer eccentric Lindblad resonance dominates. If it does, one still needs to show that this resonance can increase the global eccentricity. This is discussed in the next section.

6.10.3 Growth rate of the eccentric mode

To see if the instability would grow, consider the $m = 1$ equations. Now, driving via the products of the X_1 variables with X'_1 variables produces the desired $m = 1$ solution without time oscillations. Such driving leads to secular changes in the eccentricity terms X'_0 . Secular evolution to Order of $e\Phi_m^2$ is considered and studied by adding exponential eccentric perturbing velocities of the form

$$U'_2(r, t) = 2a(r)[e^{\lambda t} - 1]\sin(\varphi - \varpi) + b(r)e^{\lambda t}\cos(\varphi - \varpi)$$

$$V'_2(r, t) = a(r)[e^{\lambda t} - 1]\cos(\varphi - \varpi) + d(r)e^{\lambda t}\sin(\varphi - \varpi)$$

Similar to Lubow we calculate the growth rate λ for a narrow ring $[r_i, r_o]$ in the outer disk and find:

$$\lambda = \frac{1}{4a(r_o - r_i)} \left[\left(u_{nw} \frac{m+2}{2r} + \frac{du_{nw}}{dr} \right) \int_{r_i}^{r_o} v_{w,s} dr - \left(v_{nw} \frac{m-1}{2r} + \frac{dv_{nw}}{dr} \right) \int_{r_i}^{r_o} u_{w,c} dr \right] \quad (6.14)$$

Evaluating the two integrals over a narrow ring around the resonance we find:

$$\int_{r_i}^{r_o} u_{w,c} = \frac{\pi a(r_{res})}{D} \times \left([(m+1)\Omega - m\Omega_p] f(r_{res}) - 2\Omega g(r_{res}) \right)$$

$$\int_{r_i}^{r_o} v_{w,s} = \frac{\pi a(r_{res})}{D} \times \left(\Omega f(r_{res}) - 2[(m+1)\Omega - m\Omega_p] g(r_{res}) \right)$$

where

$$D = \frac{d}{dr} (\Omega^2 - [(m+1)\Omega - m\Omega_p]^2)_{r=r_{res}} \quad (6.15)$$

At the resonance location we can now write the growth rate as

$$\lambda = \frac{\pi m \Omega_p}{8(m+2)D(r_o - r_i)} [f(r_{res}) - 2g(r_{res})]^2 \quad (6.16)$$

because we can write the difference $f - 2g$ of the functions defined by Equations 6.9 and 6.10 as

$$f(r) - 2g(r) = -\frac{du_{nw}}{dr} - 2\frac{dv_{nw}}{dr} - \frac{m-1}{r} v_{nw} - \frac{m+2}{2r} u_{nw} \quad (6.17)$$

Evaluating D at $(m+2)\Omega = m\Omega_p$ for a Keplerian profile $\Omega(r) \propto r^{-3/2}$ we find that

$$D = 3m\Omega\Omega_p/r > 0 \quad (6.18)$$

This means we finally find a growth rate of:

$$\lambda = \frac{\pi m \Omega_p}{24(m)D(r_o - r_i)} [f(r_{res}) - 2g(r_{res})]^2 > 0 \quad (6.19)$$

, so we see that the resonance acts to increase the disk eccentricity.

The conclusion is that our calculations show that *if* these modes are triggered, the disk eccentricity will grow exponentially. However, one has to consider the whole set of disk modes to see when global disk eccentricity growth is possible. As mentioned in section 6.9, this is only the case for a large and deep enough gap where the surface density at the 2:1 resonance is sufficiently low. This suggests there is a threshold planetary mass above which the eccentricity growth is efficient enough to avoid being cancelled by the eccentricity damping effects present in the disk.

Previous work in Papaloizou et al. (2001) suggest this threshold mass is approximately achieved for a mass ratio of $q = 0.01$, however our simulations discussed above suggest a much lower threshold mass. In the next section we test if the phenomena we observed is indeed caused by this eccentric Lindblad resonance.

6.11 Test of the theoretical model

To analyze the growth of an eccentric instability, we define the total mode strength $S_{k,l}$ of an eccentric mode (k, l) similar to Lubow (1991b) as

$$S_{k,l} = (S_{cos,cos,k,l}^2 + S_{cos,sin,k,l}^2 + S_{sin,cos,k,l}^2 + S_{sin,sin,k,l}^2)^{1/2}$$

with $S_{f,g,k,l}$, defined in the inertial frame, given by

$$S_{f,g,k,l} = \frac{2}{\pi M(1 + \delta_{i,0})(1 + \delta_{j,0})} \int_t^{t+2\pi} dt' \int dr \int_0^{2\pi} r d\theta \\ \times \Sigma(r, \theta, t) f(i\theta) g(jt')$$

This is a measure for the current magnitude of the (k, l) -component of the eccentric perturbation. In particular, $S_{1,0}$ is a measure of the global disk eccentricity.

In the appendix of Lubow (1991b) the time derivative of the total mode strength $S_{1,0}$ is calculated and is shown to be directly related to the relevant growth mode in the inner disk, $S_{2,3}$. Similarly in the outer disk the time derivative of the $k = 1, l = 0$ mode $S_{1,0}$ is directly related to the $k = 2, l = 1$ component:

$$\frac{S_{1,0}}{dt} \propto S_{2,1} \cdot S_{1,1} \quad (6.20)$$

It is assumed in these models that $S_{1,1}$ will change much more slowly compared to the other modes and can be treated as a constant.

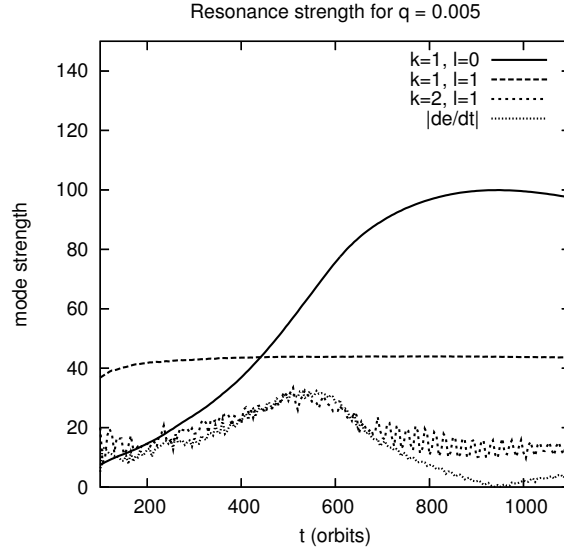


Figure 29: The strength of several modes in the disk as a function of time. The solid line refers to the global disk eccentricity $S_{1,0}$. In the exponential growth regime the time derivative of the eccentricity (dotted line) is proportional to the (2,1) wave mode (short-dashed line).

The evolution of the relevant mode strengths for a model with $q = 0.005$ is displayed in Fig. 29. The amplitude of the global eccentric mode ($k = 1, l = 0$) shows exponential growth (see Fig. 29, solid line). Furthermore, Eq. (6.20) is confirmed directly by comparing the $S_{2,1}$ -mode (short-dashed line) and the numerically obtained derivative of the eccentricity, i.e. $S_{1,0}$ (dotted curve). As it can be seen from the plot, $S_{1,1}$ is constant as suggested by the theoretical analysis of Lubow (1991a).

The good agreement of our results with theoretical expectations supports our conclusion that the mechanism for eccentricity growth is that described by Lubow (1991a) and Papaloizou et al. (2001). In our simulations growth will start after the disk has settled sufficiently and the gap has been cleared, a process which occurs on viscous time scales. Our numerical growth rates during the eccentricity increase have been estimated from the time evolution of total radial kinetic energy. In the left graph of Fig. 27 the total radial kinetic

energy of the disk is plotted as a function of time. After an initial decrease caused by the settling of the disk, the total radial kinetic energy will increase again for an eccentric disk before reaching an equilibrium. For a non-eccentric disk as for the $q = 0.002$ case (dotted line) the total radial kinetic energy will steadily decrease to an equilibrium.

By measuring the slope of the linear rising part of the curve one can measure the global eccentricity growth rate as caused by the eccentric instability discussed in this chapter. In the right graph of Fig. 27 the growth rate as a function of companion mass is plotted. A power law is a good fit to the data points and we find that the best fit is $\tau \propto M^{-2.4}$. Nevertheless for the masses considered this time scale is much shorter than the life time of the disk, and therefore this effect could be important in the evolution of massive planets.

6.12 Conclusions

We have performed numerical time dependent hydrodynamical calculations of embedded planets in viscous accretion disks. During the evolution the planet is held fixed on a circular orbit, and the whole system is evolved in time until a quasi-equilibrium state has been reached. In contrast to previous existing simulations on this problem we have extended the evolutionary time to several thousand orbits of the embedded planet for a whole range of different planetary masses.

We find that beyond a certain critical mass of the planet the structure of the disk changes from a circular to an eccentric state. For typical viscosities in protoplanetary disks $\nu = 10^{-5}$ (or $\alpha \approx 0.004$) the transition to the eccentric case occurs already for critical masses of $M_p = 3M_{Jup}$. Through a modal analysis we demonstrate that the eccentric ($k = 1, l = 0$) mode in the disk is indeed driven by the ($k = 2, l = 1$) wave mode which is excited at the outer 1:3 Lindblad resonance. The numerically inferred growth rate of the unstable eccentric disk mode is roughly proportional to M_p^n with $n = 2.4$, which is slightly larger than the predicted value of $n = 2.0$ (Lubow 1991a; Papaloizou et al. 2001). The discrepancy is most likely due to a change in the density structure of the gap for different planetary masses. For small masses $M_p = 2M_{Jup}$ no eccentricity growth has been found. Here the damping effects of

disk viscosity and pressure keep the disk in the circular state. Upon increasing the planetary mass the eccentricity eventually saturates at a value of $e \approx 0.25$.

The excitation of eccentric disk modes by massive companions has been studied within the framework of Cataclysmic Variable stars as an instability of the inner disk (Lubow 1991a,b). In those cases the change in viscous dissipation induced by the slow precession of the disk is presently the preferred mechanism to explain the observed Superhumps in the light curve of some systems. That the same process is also applicable to (outer) disks around an embedded protoplanet has been confirmed by Papaloizou et al. (2001) in their study of very massive planets. In their simulations a much larger threshold mass ($\approx 10 - 20M_{\text{Jup}}$) has been found. However, their simulations were run only for 800 planetary orbits or less, which is not sufficient to see growth for small mass planets considering the long growth time of the eccentric mode.

The change in the state of the disk has significant consequences for the mass accretion rate onto the planet. For circular disks the width of the gap widens upon an increase in the planetary mass which shuts off eventually further accretion of disk material. The maximum mass a planet may reach by this process is around $5M_{\text{Jup}}$ (Bryden et al. 1999; Lubow et al. 1999). We suggest that through the excitation of the eccentric mode in the disk the planet can reach larger masses more readily, as there are quite a few systems with (minimum) planetary masses larger than $5M_{\text{Jup}}$. The influence an eccentric disk might have on the evolution of a pair of planets engaged in a 2:1 resonance has been analyzed recently by Kley et al. (2005). Here, changes in the libration amplitude of the resonant angles are to be expected.

It has been suggested that the gravitational back reaction of an embedded planet with the surrounding disk can lead to an increase in the orbital eccentricity of the planet (Goldreich and Sari 2003; Ogilvie and Lubow 2003), and may serve as a possible mechanism to explain the observed high eccentricities in extrasolar planetary systems. In the present work the gravitational back reaction of such an eccentric disk on the planetary orbit has not been analyzed, and remains to be studied in the future. The magnitude of the reachable eccentricity depends on the absolute physical mass of the ambient disk. Through numerical simulations Papaloizou et al. (2001) find that a significant increase in planetary

eccentricity is only seen for a planet mass above $10 M_{Jup}$. However, even in this case the maximum eccentricities do not increase beyond $e = 0.25$. Additionally, the evolution time of the models was very short and did not allow to study the long term evolution of the eccentricity.

As the effect of disk eccentricity scales with planet mass at least as $\propto M_p^{2.4}$ the effect is most pronounced for very massive planets. However, in that case it is also more difficult to induce high planetary eccentricities. Hence, it is very questionable if the back reaction of the disk can produce the observed high eccentricities found in the surveys.

The present study is only two dimensional and has not included any thermal effects such as radiative cooling or transport. Since in two dimensional calculations the gravitational effect between planet and disk tends to be overestimated (as the disk is confined to the equatorial plane) one might expect a reduced effect in full three-dimensional simulations. But the very low value of the critical transition mass leaves sufficient room for an importance of this effect in the growth of extrasolar planets.

7 Simulations with a moving planet

Part of the inhumanity of the computer is that, once it is competently programmed and working smoothly, it is completely honest.

- Isaac Asimov

Although up to this point we have looked at planets in fixed orbits around the central star, a planet embedded in a disk will interact with the disk as described in chapter 3 and thus change its orbit. This chapter discusses numerical simulations where the planet is allowed to change its orbit. In particular, the initial condition need not be a circular coplanar orbit. The details of how the planet orbit is calculated can be found in section 4.3. The chapter will be divided into two parts. First we look at the linear regime as defined in 3.3: planets with a very low mass that can be treated as a small perturbation of the potential and experience Type I migration. Then we look at the other extreme: The orbital evolution of planets that cause an eccentric disk as described in chapter 6.

7.1 Low mass

For these simulations we have looked at planets with a very low mass compared to the other calculations we present here: 20 Earth masses, or a mass ratio of $q = 6 \times 10^{-5}$. Planets of this mass are in the regime of Type-I migration and show fast orbital evolution and are therefore especially well suited to see quick effects. Also, planets of this mass are approximately the lowest mass planets found outside our Solar System at the time of writing, some at orbits of only several days.

This work has been done in collaboration with Paul Cresswell and Richard Nelson, both at Queen Mary University of London, Astronomy Unit.

7.1.1 Initial setup

We use the initial setup as described in section 5.1.2, but with an initial surface density profile that falls off as $\Sigma(r) \propto r^{-1/2}$. As the planet is now interacting

with the protoplanetary disk, the disk mass is relevant. The total disk mass inside the computational domain [$r_{min} = 0.4a, r_{max} = 2.5a$] is $m_{tot} = 0.007$ Solar masses. The unit of distance and initial semimajor axis of the planet is similar that of Jupiter: $a_0 = 5.0AU$

7.1.2 Eccentricity and Inclination damping

As for orbital migration, one can deduce formulae for the eccentricity evolution of a planet embedded in a gaseous disk. As shown in Tanaka and Ward (2004) and Tanaka and Ida (1996), the instantaneous eccentricity and inclination change due to forces from the disk on the planet under the local approximation (or so-called Hill approximation), see section 4.3, is given by

$$\dot{e} = \frac{1}{M_p \Omega_p a} \left[F_r \sin(\Omega_p t - \varpi) + 2F_\theta \cos(\Omega_p t - \varpi) \right]$$

where ϖ is the longitude of periastron. Similarly, the instantaneous inclination change is given by

$$di/dt = \frac{1}{M_p \Omega_p A} F_z \cos(\Omega_p t - \psi)$$

where ψ is longitude of the ascending node. Using this one can calculate the theoretical eccentricity damping time $t_e = e/|de/dt|$ for an embedded planet. Papaloizou and Larwood (2000) find that $\dot{e} < 0$ and show that one can distinguish two extreme cases: Low eccentricity ($e < H/r$) and high eccentricity ($e > H/r$). In the first case, for small eccentricities, t_e is constant, in other words the orbital eccentricity of the planet will decay exponentially.

In the high eccentricity case $t_e \propto e^3$. For our calculations this means if $e(0) = e_0 \gg H/r$ then $e(t)$ is of the form $C_1 - C_2 t^{1/3}$. In general they find a formula that is valid over the whole regime:

$$t_e \propto 1 + \frac{1}{4} \left(\frac{e}{H/r_0} \right)^3$$

The behavior of the inclination is similar to that of the eccentricity: It is shown in Tanaka and Ward (2004) that the damping time t_i is constant for small inclinations, i.e. inclinations at which the planet does not leave the disk ($i < H/r$). If the planet leaves the disk ($i > H/r$), damping slows down. A behavior similar to that of the eccentricity damping results can be observed:

Although not proven theoretically the inclination damping curve fits well to $di/dt/i \propto i^3$ for $i > H/r$.

7.1.3 Numerical setup

We consider our standard model as described above with a planet mass of $q = 6 \times 10^{-5}$ and an initial eccentricity ranging from $e = 0$ to 0.3. We allow the planet to migrate due to the torques exerted on it by the disk. We run the models until we find no more significant evolution in the eccentricity of the planet.

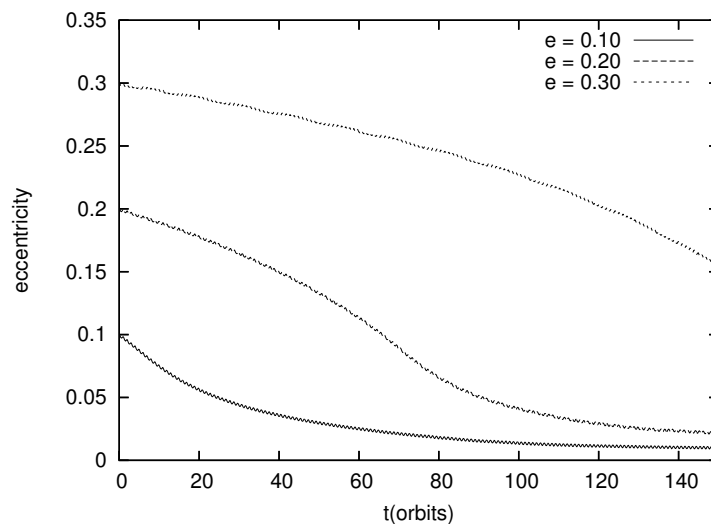


Figure 30: Eccentricity as a function of time for different initial eccentricities. We find exponential growth in the low-eccentricity regime and slower damping for higher eccentricities.

7.1.4 Low initial eccentricity

If we start with a sufficiently low eccentricity ($e_0 < 0.1$) we observe a decay of the orbital eccentricity of the planet. $e(t)$ for several different initial eccentricities is shown in Fig. 30. In Fig. 31 we study the migration rate of a planet on a low-eccentricity orbit. Notice that for the circular orbit ($e_0 = 0$) we maintain a near-circular orbit.

The decay of the planet eccentricity in these cases can be fitted to a theoretical model with $\dot{e}/e = \text{constant}$, or exponential decay. We find that for these particular models, the damping time is approximately 30 orbits. As this is

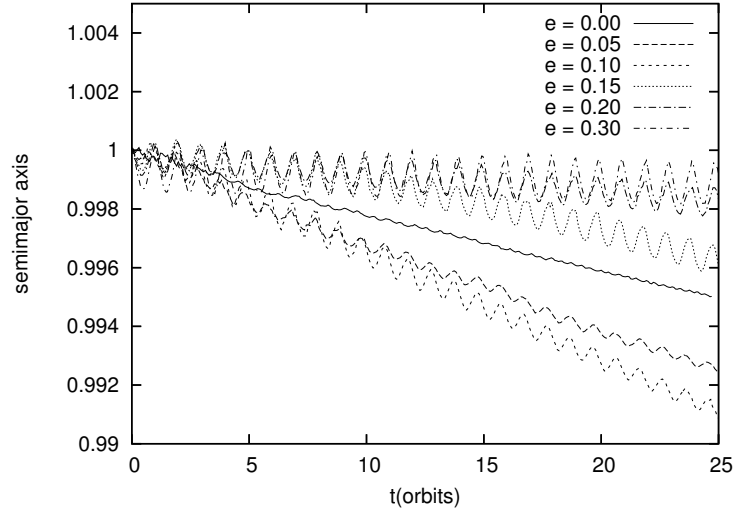


Figure 31: Semi-major axis of the planet as a function of time for different initial eccentricities. For small non-zero eccentricities the migration rate increases, for large eccentricities the migration rate approaches zero.

much smaller than the migration time scale, we can assume that such damping is instantaneous, i.e. a small perturbation from external forces will be compensated very quickly without changing the orbit or the growth of the planet significantly.

As shown analytically in Tanaka and Ward (2004) the eccentricity and inclination damping of the planet orbit is caused by eccentric bending waves in the disk. The damping time scale is given by

$$\dot{\bar{e}}/e = -\frac{0.780}{t_{wave}} \quad (7.1)$$

with characteristic time

$$t_{wave} = q^{-1} \left(\frac{\sigma_p a^2}{M_*} \right)^{-1} \left(\frac{c_s}{a \Omega_p} \right)^4 \Omega_p^{-1} \quad (7.2)$$

with q the mass ratio between the planet and the star, and σ_p the local surface density at the planet radius. For a planet of 20 Earth masses at 5 AU in a MMSN nebula ($\sigma = 1280 \text{ kg m}^{-2}$), as in our model, the characteristic time $t_{wave} = 425 \text{ yr} = 46 \text{ orbits}$. This gives an eccentricity damping time scale of 59 orbits. The best estimate of the eccentricity damping time scale for the simulations shown in Fig. 30 is 35 orbits. Although this is a bit lower it is of the same order of magnitude as the theoretical prediction.

An interesting effect can be seen when one looks at the migration time scale of the planet. For these low eccentricities we find a slightly faster migration rate for the planet than in the circular case. However, if the eccentricity is larger than a certain value (the high eccentricity case), this effect is reversed. It is not clear what is the cause of this increase in migration rate. On the other hand, the decrease of the migration rate for high eccentricities can be understood: because of the large velocity difference between the planet and the surrounding disk material, the strength of the spiral waves will decrease as their location changes constantly, and this perturbation will cause a smaller back reaction on the planet.

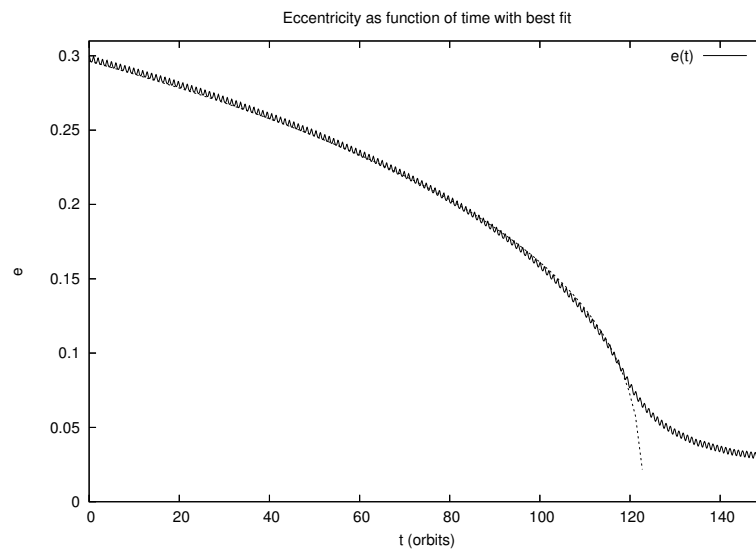


Figure 32: The model with $e_0 = 0.3$ is fitted to a theoretical model which predicts $\dot{e} \propto e^{-2}$. As can be seen this model works extremely well as long as the eccentricity is larger than H/r .

7.1.5 High initial eccentricity

If we start with a high initial eccentricity ($e_0 > 0.1$) we also observe a decay of the orbital eccentricity of the planet, but it is slower and not exponential. It fits well to the theoretical model, which predicts $\dot{e} \propto e^{-2}$. In Fig. 32 the numerical calculation with $e_0 = 0.3$ is fitted with such a model. The fit is extremely good. Also notice that up to the point where exponential decay sets in, the different curves are time-shifted copies of each other, which means that any previous evolution can not be recognized in the current eccentricity evolution

curve. After exponential decay is reached there is a residual eccentricity that does not go away. This most likely has to do with material that is very near to the planet.

For these high eccentricities we find a decreased migration rate, which can be explained by the large velocity difference between the planet and the surrounding material. This velocity difference diminishes the strength of the spiral waves that are causing the migration. We also find a sharp increase of the migration rate as soon as the eccentricity becomes smaller than 0.1 for these models. In Figure 33 the relative migration rate compared to the $e = 0$ model is plotted. For small eccentricities the migration rate may increase by as much as 60% before dropping off as expected for larger eccentricities. For a very large eccentricity of $e = 0.3$ the migration rate is 5 times smaller than for the same planet on a circular orbit.

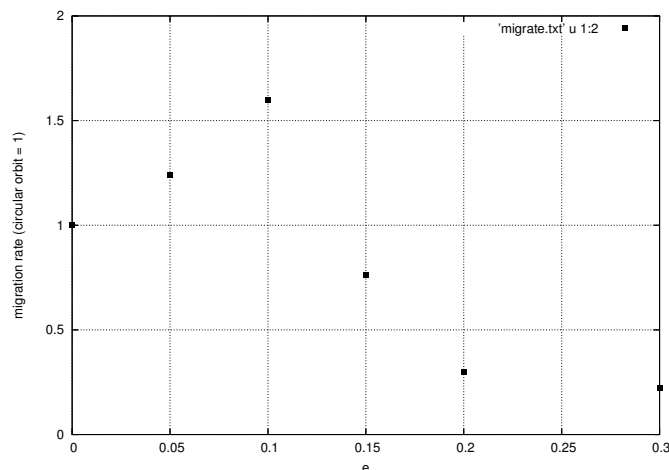


Figure 33: The relative migration rate as a function of eccentricity for a planet with $q = 6 \times 10^{-5}$. For low eccentricities the migration rate may increase by up to 60%, for high eccentricities we find very slow orbital migration.

In the long term evolution of the migration rate we see in Figure 34 that all models converge to the circular migration rate when approaching $e = 0$, as expected. For the $e = 0.3$ model the eccentricity has not dropped enough to reach the changeover from the slow migration regime (large e) to the slow migration regime (small nonzero e), but will eventually reach the same migration rate as the other models (see also the two-dimensional model in section 7.1.6).

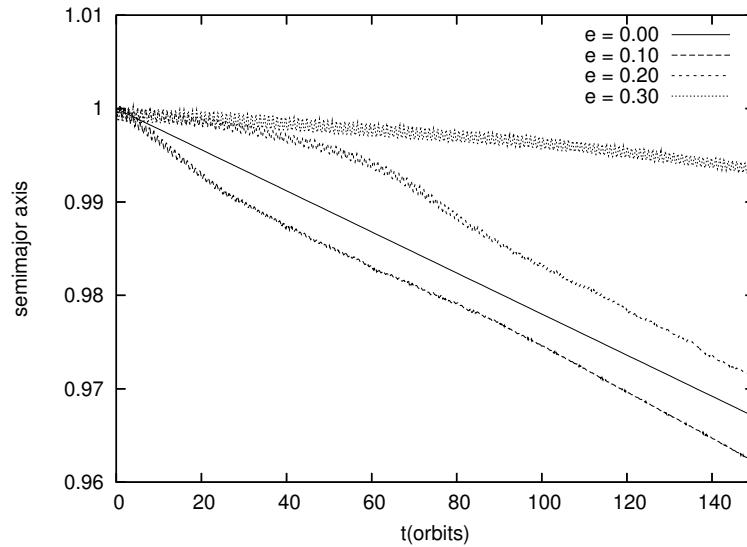


Figure 34: The long term evolution of the semimajor axis for different initial eccentricities. All models except the one with the largest initial eccentricity converge to the same migration rate.

7.1.6 Comparison to two-dimensional models

To investigate the effect of the lack of a third dimension, we have performed all the models with a low mass eccentric planet in a two-dimensional setup as well. Our initial conditions are exactly as in the models for three dimensions, vertically averaged. The grid structure is the one used in section 5.1.1. The evolution of the orbital elements of a 20 Earth-mass planet starting on an eccentric orbit with initial eccentricity between 0 and 0.3 for the two-dimensional models is shown in Figure 35. In the top panel the semimajor axis is shown. With the correct treatment of the potential smoothing as described in section 4.7.2, the migration rate in the two-dimensional case is equal to the migration rate in three dimensions. Also, as can be seen from the semimajor axis at $t = 250$ orbits, the models with $e_0 = 0.05$ and $e_0 = 0.10$ have migrated the most as in the three-dimensional case. Another feature that is preserved from the three-dimensional calculations is the sharp change in migration rate when the eccentricity drops below 0.15. For the $e_0 = 0.30$ model this happens after approximately 220 orbits, for the $e_0 = 0.20$ model after approximately 60 orbits.

There are also some distinct differences. The most important difference is

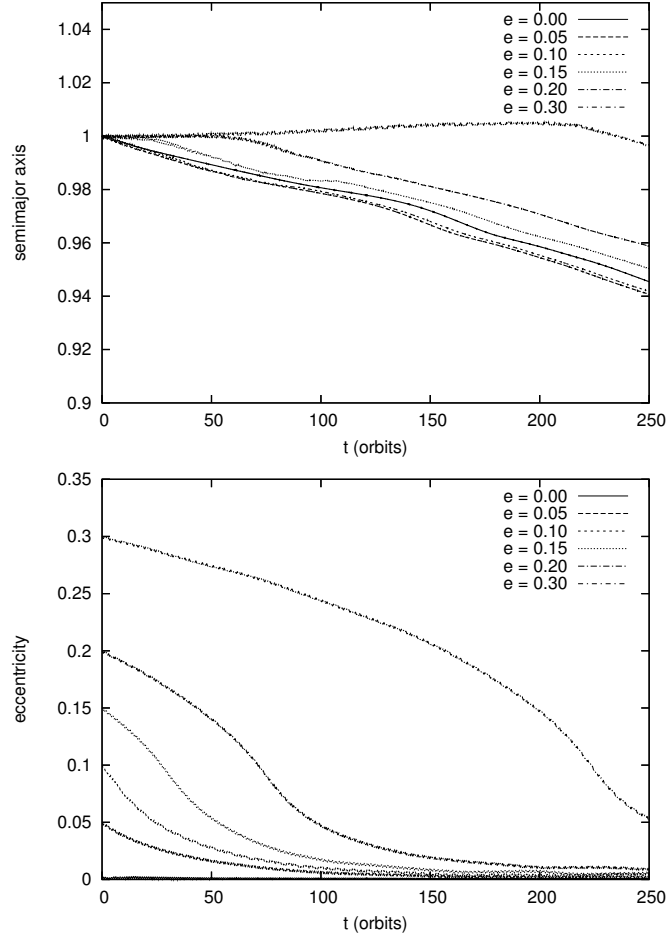


Figure 35: **top)** Semi-major axis as a function of time for $q = 6 \times 10^{-5}$ in two-dimensional calculations. For very high eccentricities the direction of migration is reversed. **bottom)** Eccentricity as a function of time for $q = 6 \times 10^{-5}$ in two-dimensional calculations. The models show exactly the same features as the corresponding models in three dimensions.

the sign of the migration rate. In the two-dimensional case we get outward migration for high eccentricities, whereas in the three-dimensional case even for the high eccentricities ($e > 0.15$) migration was still inward. In the bottom panel of Figure 35 the eccentricity is plotted as a function of time. Both the damping time scale and the dependency of the damping rate on the actual eccentricity are the same as in three dimensions.

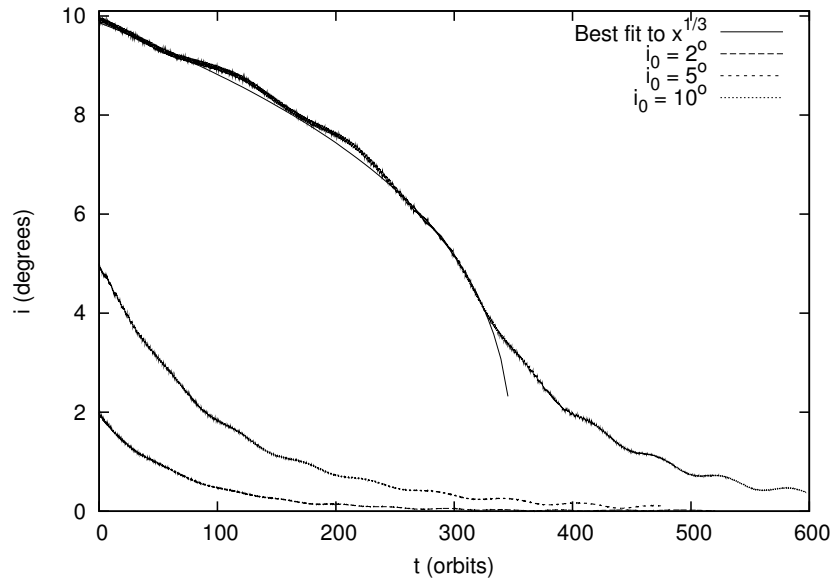


Figure 36: Inclination as a function of time for different initial values of i . We find exponential decay as long as $i < H/r$. For higher eccentricities the damping time scale increases dramatically. A good fit is found with a model with $di/dt \propto i^{-2}$

7.1.7 Inclination damping

If we start with a planet on a circular but inclined orbit the inclination will be damped. The time scale for inclination damping is significantly longer than the eccentricity damping time scale. Again we find two different regimes. For $i < H/r$ the planet will stay inside the disk and the damping is exponential: $di/dt \propto i$. The damping time scale for a small planet mass and small inclinations is given in Tanaka and Ward (2004) as:

$$\frac{\dot{i}}{i} = -\frac{0.544}{t_{wave}} \quad (7.3)$$

with t_{wave} defined as in 7.2. For our simulations this would give a damping time scale of 85 orbits. The two lower curves in Fig. 36 shows the inclination damping for small initial inclinations (2° and 5° respectively) and a measurement of the damping rate suggests an inclination damping time scale of approximately 70 orbits, so just as for the eccentricity we find very good agreement with analytical results.

For higher inclinations we find a slower inclination damping rate as can be seen in Fig. 36. The best fit to the model with the highest initial inclination of

10° is one with $di/dt \propto i^{-2}$. This is equal to the behavior of the eccentricity damping rate for large eccentricities.

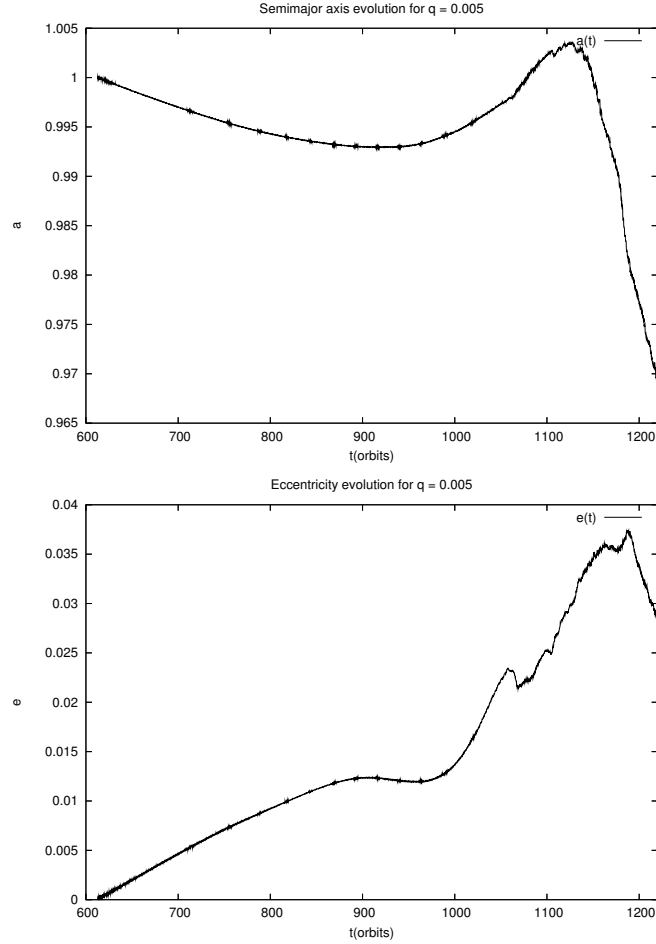


Figure 37: **top**) Semi-major axis as a function of time for $q = 0.005$ in an eccentric disk. At some point migration is reversed and goes outward instead of inward. **bottom**) Eccentricity as a function of time for $q = 0.005$ in an eccentric disk. The eccentric disk causes rise in the orbital eccentricity of the planet. As a comparison, models without an eccentric disk and a planet on a circular orbit will keep the planet on a circular orbit.

In case of a nonzero inclination we find that the migration rate is unaffected by the inclination for $i < 10^\circ$, in other words the migration rate is the same as for the models without inclination, regardless of the initial eccentricity (for $e_0 = 0, 0.05$ or 0.10).

7.2 Eccentric disks and orbital elements

With a planet mass of 5 Jupiter masses, enough to create an eccentric disk on a computationally feasible time scale, one can of course hope for eccentricity growth for the planetary orbit once the disk has become eccentric. However the disk mass will now be of the same order as the planet mass, so quick changes in the orbital parameters of the planet are not expected. One must also be careful not to create numerical artifacts by moving around a very massive planet too quickly.

For these calculations we started with an eccentric disk model from the previous chapter and ran it until it reached an eccentric disk state. At this point the back reaction of the disk onto the planet is activated. The planet will migrate and, since the disk is eccentric, the expectation is that the orbital eccentricity of the planet will become systematically nonzero. This would then be significantly different than for the normal equilibrium mode of the disk. For example for $q = 0.001$ we find no eccentricity growth if we start with a planet on a circular orbit, only a residual eccentricity caused by small variations in the force on the planet of the order of 10^{-3} .

The orbital evolution of such a system for a planetary mass of $q = 0.005$ is shown in Fig. 37. In the top panel the semimajor axis is plotted, in the bottom panel the eccentricity. Since the mass of the planet is of the same order as that of the part of the disk inside of the computational domain, evolution is slow as expected.

The first 200 orbits we can observe a steady inward migration and a steady rise in eccentricity. This is in contrast to calculations where there is no eccentric disk regardless of the planet mass, as for such calculation we find only small short-term variations of the eccentricity that are quickly damped out. After about 300 orbits of evolution the direction of migration changes due to the interaction between the planet and the disk, and after this the interaction becomes more intimate. During this evolution the eccentric state of the disk is preserved, leading to the conclusion that the situation where a massive planet is embedded in an eccentric disk leads to a non-circular orbit for the planet. Finally at about $t = 1100$ orbits a second reversal of the migration rate takes place, at this point the eccentricity is about $e = 0.035$. The planet now moves

into a fast-migrating mode. At this point the accuracy of the simulation decreases because of the quick changes of the semimajor axis. At this point the various simulations we have performed show varying behavior of the orbital eccentricity: In some simulations the eccentricity quickly increases to $e = 0.2$, in some others it will remain around $e = 0.05$. As the results depend so heavily on small changes in the initial conditions we will not give rigid conclusions on the final orbital eccentricity of the planet.

The observed non-circularity of the planetary orbit in these simulations is not of the size of the large eccentricities observed for extra-solar planets (the average observed eccentricity for extrasolar planets is $e = 0.3$, see chapter 2) but a massive planet on a non-circular orbit can be the starting point of planet - planet interaction, which may lead to larger eccentricities in itself. Another possibility is that the eccentric disk caused by the massive planet may increase the orbital eccentricity of other planets in the system.

7.3 Conclusions

We have performed 3-dimensional numerical simulations of a planet in a protoplanetary disk. The planet was allowed to change its orbit. We investigated the orbital evolution of the planet in two mass regimes. In the low mass regime we are in the linear regime in which detailed analytical results are known. For small eccentricities and inclinations good agreement is found between our results and linear theory. Also in the case of large eccentricities the slower decrease of e is well understood.

For the migration rates as a function of eccentricity we find some surprising results: For low eccentricities we find faster migration than in the case of zero eccentricity - an increase of up to 60% is observed - before migration slows down as expected for higher eccentricities.

We have also performed a comparative study of these models in two dimensions and find good agreement in the migration and eccentricity damping rate. Also the increased migration for small non-zero eccentricities is reproduced. However, in two dimensions the migration rate for high-eccentricity planets is reversed unlike in the three-dimensional case.

Additionally we studied the inclination damping for low-mass embedded

planets. If the initial inclination of the planet is small enough we find a rapid exponential decay, however if the initial inclination is larger than the scale height of the disk, the damping rate decreases dramatically.

For higher mass planets we enter the non-linear regime. As shown in Chapter 6, very high mass planets cause eccentricity growth in the disk. In this Chapter we couple this to eccentricity growth of the planet orbit. For an initial eccentricity $e_0 = 0$ we find eccentricity growth for those planets that create an eccentric disk, something not found in any other mass range. We think that this is an important mechanism to introduce eccentricity into the system, and it may not only affect the planet causing the perturbations in the disk but also other planets.

8 Conclusions

There is a theory which states that if ever anybody discovers exactly what the Universe is for and why it is here, it will instantly disappear and be replaced by something even more bizarre and inexplicable. There is another theory which states that this has already happened.

- Douglas Adams

This chapter summarizes the research findings of this thesis on planet-disk interaction with planets on a fixed orbit, first for Neptune and Jupiter mass planets and then beyond, and planets on a dynamic orbit, also here for low- and high-mass planets.

8.1 Fixed planet orbits

We have performed a comparison between many different numerical codes as described in Chapter 5, and our contribution agrees well with the other contributions with similar codes. In addition we have performed a resolution study and found that although the results look promising at the lowest resolution, slight differences can be detected for higher resolutions. This is a hint that although most conclusions from the low-resolution studies will be correct, one should treat them with care.

We feel that this comparison project has provided a good benchmark for others writing a code that intends to deal with this particular problem.

Extending the parameter space set by the comparison problem we have found a special disk state for high-mass embedded planets that may help explain the existence of such planets by virtue of the increased accretion rate in our models, which is urgently needed to allow such planets to form before the protoplanetary disk dissipates. This eccentric state is robust and theoretically sound but since the evolution to such a state takes a long time, it is no surprise that it has not been observed before for such low planet masses.

8.2 Moving planet

We have looked at the eccentricity and inclination evolution for low-mass moving planets in Chapter 7 and found good agreement with theoretical analysis. This is useful for others planning to do research in this area since we can conclude that planets subject to type I migration can be assumed to move on a coplanar, circular orbit, as long as no other effects like a second planet or a close encounter with a star are relevant.

The picture is much different for planets with very high masses as can be seen in Chapter 7.2. These cause an eccentric outer protoplanetary disk and in turn the eccentric disk forces the planet from its circular orbit into an eccentric one. This non-zero eccentricity $0 < e < 0.1$ is not of the same order of magnitude as the observed eccentricities of many extrasolar planets but once this state has been reached both the planet and the disk may influence other planets in the system as well.

8.3 Future work

It is still a long way to fully understanding the interactions between a protoplanetary disk and the embedded protoplanet. There are many aspects which have not been touched in this thesis, for example using high-resolution methods to zoom in in the region of the planet and the inclusion of more physics: The addition of radiative transfer and magnetic fields.

First the addition of radiative transfer may have a large impact on the area near to the planet. When the surroundings of the planet are heated up by the hot accreting planet, this will change the local density distribution and as such may influence the planet migration. There has already been some work in this area, mostly about the observability of embedded planets, see for example Wolf et al. (2002).

Second, the inclusion of magnetic fields as discussed in section 3.5.1 will also change the migrational behavior of a planet.

Another interesting problem arises when one looks at planets of intermediate masses: those that open a gap but are not massive enough to excite eccentricity in the disk (for example Jupiter). It is very hard to make analytic

prediction on the behavior of the orbital eccentricity and inclination of such a planet, and unfortunately also very hard to get consistent results in numerical simulations of this problem.

Another possible problem that has become solvable with the current increased computer power is to try to reproduce the final state of a forming planetary system: What happens to the planets in the disk dispersal phase? Especially for this aspect also multiple planet systems need to be considered. Since the disk dispersal needs to last for many thousands of orbits, this problem is computationally challenging. But at some point one needs to solve this problem to be able to say something about the space of possible planetary systems and the possible scenarios to form them.

References

- Artymowicz, P., 1992. Dynamics of binary and planetary-system interaction with disks - Eccentricity changes. *PASP* 104, 769–774.
- Balbus, S. A., Hawley, J. F., 1991. A powerful local shear instability in weakly magnetized disks. I - Linear analysis. II - Nonlinear evolution. *ApJ* 376, 214–233.
- Bally, J., Testi, L., Sargent, A., Carlstrom, J., 1998. Disk Mass Limits and Lifetimes of Externally Irradiated Young Stellar Objects Embedded in the Orion Nebula. *Astron. Journal* 116, 854–859.
- Barman, T. S., Hauschildt, P. H., Allard, F., 2001. Irradiated Planets. *ApJ* 556, 885–895.
- Bennett, D. P., PLANET Collaboration, OGLE Collaboration, MOA Collaboration, 2005. Discovery of a Cool, Low-Mass, Extra-solar Planet by Gravitational Microlensing. *American Astronomical Society Meeting Abstracts* 207.
- Berlage, H. P., 1934. A study of the systems of satellites from the standpoint of the disc- theory of the origin of the planetary system. *Annals of the Bosscha Observatory Lembang (Java) Indonesia* 4, 79.
- Boss, A. P., 1999. Giant Planet Formation by Disk Instability. In: *Lunar and Planetary Institute Conference Abstracts*, pp. 1049.
- Brown, T. M., Charbonneau, D., Gilliland, R. L., Noyes, R. W., Burrows, A., 2001. Hubble Space Telescope Time-Series Photometry of the Transiting Planet of HD 209458. *ApJ* 552, 699–709.
- Bryden, G., Chen, X., Lin, D. N. C., Nelson, R. P., Papaloizou, J. C. B., 1999. Tidally Induced Gap Formation in Protostellar Disks: Gap Clearing and Suppression of Protoplanetary Growth. *ApJ* 514, 344–367.
- Bryden, G., Różyczka, M., Lin, D. N. C., Bodenheimer, P., 2000. On the Interaction between Protoplanets and Protostellar Disks. *ApJ* 540, 1091–1101.

- Charbonneau, D., Brown, T. M., Latham, D. W., Mayor, M., 2000. Detection of Planetary Transits Across a Sun-like Star. *ApJ* 529, L45–L48.
- Crifo, F., The Gaia Team, 2004. The ESA mission GAIA. In: Combes, F., Barret, D., Contini, T., Meynadier, F., Pagani, L. (Eds.), *SF2A-2004: Semaine de l’Astrophysique Francaise*, pp. 281.
- D’Angelo, G., Henning, T., Kley, W., 2002. Nested-grid calculations of disk-planet interaction. *A&A* 385, 647–670.
- de Val Borro, M., *subm.* A comparative study of disc-planet interaction. *MNRAS*.
- Fortney, J. J., Sudarsky, D., Hubeny, I., Cooper, C. S., Hubbard, W. B., Burrows, A., Lunine, J. I., 2003. On the Indirect Detection of Sodium in the Atmosphere of the Planetary Companion to HD 209458. *ApJ* 589, 615–622.
- Fridlund, C. V. M., Capaccioni, F., 2002. Infrared space interferometry - the DARWIN mission. *Advances in Space Research* 30, 2135–2145.
- Goldreich, P., Sari, R., 2003. Eccentricity Evolution for Planets in Gaseous Disks. *ApJ* 585, 1024–1037.
- Goldreich, P., Tremaine, S., 1979. The excitation of density waves at the Lindblad and corotation resonances by an external potential. *ApJ* 233, 857–871.
- Goldreich, P., Tremaine, S., 1981. The origin of the eccentricities of the rings of Uranus. *ApJ* 243, 1062–1075.
- Hartmann, W. K., 1968. Growth of Asteroids and Planetesimals by Accretion. *ApJ* 152, 337–342.
- Henning, T., Ilgner, M., 2003. Chemistry and Transport in Accretion Disks. In: Curry, C. L., Fich, M. (Eds.), *SFChem 2002: Chemistry as a Diagnostic of Star Formation*, proceedings of a conference held August 21-23, 2002 at University of Waterloo, Waterloo, Ontario, Canada N2L 3G1. Edited by Charles L. Curry and Michel Fich. NRC Press, Ottawa, Canada, 2003, p. 54., pp. 54.

- Kargel, J. S., 1987. Mass Distributions in Minimum Mass Models of the Jovian, Saturnian, Uranian, and Solar Nebulae. In: Lunar and Planetary Institute Conference Abstracts, pp. 477.
- Kessler-Silacci, J. E., C2d Irs Team, 2005. c2d Spitzer-IRS Spectra of Disks Around T Tauri Stars: Silicate Emission and Grain Growth. In: Protostars and Planets V, Proceedings of the Conference held October 24-28, 2005, in Hilton Waikoloa Village, Hawai'i. LPI Contribution No. 1286., p.8186, pp. 8186.
- Kley, W., 1989. Radiation hydrodynamics of the boundary layer in accretion disks. I - Numerical methods. *A&A* 208, 98–110.
- Kley, W., 1998. On the treatment of the Coriolis force in computational astrophysics. *A&A* 338, L37–L41.
- Kley, W., 1999. Mass flow and accretion through gaps in accretion discs. *MNRAS* 303, 696–710.
- Kley, W., Dirksen, G., 2006. Disk eccentricity and embedded planets. *A&A* 447, 369–377.
- Kley, W., Lee, M. H., Murray, N., Peale, S. J., 2005. Modeling the resonant planetary system GJ 876. *A&A* 437, 727–742.
- Konacki, M., 2005. Precision Radial Velocities of Double-lined Spectroscopic Binaries with an Iodine Absorption Cell. *ApJ* 626, 431–438.
- Lewis, G. F., 2001. Gravitational microlensing of stars with transiting planets. *A&A* 380, 292–299.
- Lissauer, J. J., Stewart, G. R., 1991. Growth of planets from planetesimals. Technical report.
- Lubow, S. H., 1991a. A model for tidally driven eccentric instabilities in fluid disks. *ApJ* 381, 259–267.
- Lubow, S. H., 1991b. Simulations of tidally driven eccentric instabilities with application to superhumps. *ApJ* 381, 268–277.

- Lubow, S. H., Seibert, M., Artymowicz, P., 1999. Disk Accretion onto High-Mass Planets. *ApJ* 526, 1001–1012.
- Malbet, F., Lachaume, R., Monin, J.-L., Berger, J.-P., 2000. Probing the inner part of protoplanetary disks with the VLTI. In: Lena, P. J., Quirrenbach, A. (Eds.), *Proc. SPIE Vol. 4006*, p. 243-251, *Interferometry in Optical Astronomy*, Pierre J. Lena; Andreas Quirrenbach; Eds., pp. 243–251.
- Marcy, G., Butler, R. P., Fischer, D., Vogt, S., Wright, J. T., Tinney, C. G., Jones, H. R. A., 2005. Observed Properties of Exoplanets: Masses, Orbits, and Metallicities. *Progress of Theoretical Physics Supplement* 158, 24–42.
- Marcy, G. W., Butler, R. P., Fischer, D., Vogt, S. S., Lissauer, J. J., Rivera, E. J., 2001. A Pair of Resonant Planets Orbiting GJ 876. *ApJ* 556, 296–301.
- Marcy, G. W., Butler, R. P., Vogt, S. S., Fischer, D., Liu, M. C., 1999. Two New Candidate Planets in Eccentric Orbits. *ApJ* 520, 239–247.
- Masset, F. S., 2001. On the Co-orbital Corotation Torque in a Viscous Disk and Its Impact on Planetary Migration. *ApJ* 558, 453–462.
- Masset, F. S., Papaloizou, J. C. B., 2003. Runaway Migration and the Formation of Hot Jupiters. *ApJ* 588, 494–508.
- Mayor, M., Queloz, D., Marcy, G., Butler, P., Noyes, R., Korzennik, S., Krockenberger, M., Nisenson, P., Brown, T., Kennelly, T., Rowland, C., Horner, S., Burki, G., Burnet, M., Kunzli, M., 1995. 51 Pegasi. *IAU Circ.* 6251, 1.
- Mizuno, H., 1980. Formation of the Giant Planets. *Progress of Theoretical Physics* 64, 544–557.
- Muzerolle, J., Young, E. T., Megeath, S. T., Lada, C., MIPS Team, Irac Team, 2004. Protoplanetary Disk Evolution: Early Results from Spitzer. In: Krot, A., Scott, E., Keil, K., Reipurth, B. (Eds.), *Workshop on Chondrites and the Protoplanetary Disk*, pp. 9081.
- Nakazawa, K., Ida, S., 1988. Hill’s approximation in the three-body problem. *Progress of Theoretical Physics Supplement* 96, 167–174.

- Nelson, R. P., Papaloizou, J. C. B., 2004. The interaction of giant planets with a disc with MHD turbulence - IV. Migration rates of embedded protoplanets. *MNRAS* 350, 849–864.
- Nelson, R. P., Papaloizou, J. C. B., Masset, F. S., Kley, W., 2000. The migration and growth of protoplanets in protostellar discs. *MNRAS* 318, 18–36.
- Neuhäuser, R., Guenther, E. W., Wuchterl, G., Mugrauer, M., Bedalov, A., Hauschildt, P. H., 2005. Evidence for a co-moving sub-stellar companion of GQ Lup. *A&A* 435, L13–L16.
- Ogilvie, G. I., Lubow, S. H., 2003. Saturation of the Corotation Resonance in a Gaseous Disk. *ApJ* 587, 398–406.
- Papaloizou, J. C. B., Larwood, J. D., 2000. On the orbital evolution and growth of protoplanets embedded in a gaseous disc. *MNRAS* 315, 823–833.
- Papaloizou, J. C. B., Nelson, R. P., 2003. The interaction of a giant planet with a disc with MHD turbulence - I. The initial turbulent disc models. *MNRAS* 339, 983–992.
- Papaloizou, J. C. B., Nelson, R. P., Masset, F., 2001. Orbital eccentricity growth through disc-companion tidal interaction. *A&A* 366, 263–275.
- Perryman, M. A. C., 2000. Extra-solar planets. *Reports of Progress in Physics* 63, 1209–1272.
- Press, W. H., Teukolsky, S. A., Vetterling, W. T., Flannery, B. P., 1992. *Numerical recipes in FORTRAN. The art of scientific computing*. Cambridge: University Press, —c1992, 2nd ed.
- Santos, N. C., Benz, W., Mayor, M., 2005. Extrasolar Planets: Constraints for Planet Formation Models. *Science* 310, 251–255.
- Sari, R., Goldreich, P., 2004. Planet-Disk Symbiosis. *ApJ* 606, L77–L80.
- Setiawan, J., Rodmann, J., da Silva, L., Hatzes, A. P., Pasquini, L., von der Lühe, O., de Medeiros, J. R., Döllinger, M. P., Girardi, L., 2005. A substellar companion around the intermediate-mass giant star HD 11977. *A&A* 437, L31–L34.

- Stone, J. M., Norman, M. L., 1992. ZEUS-2D: A radiation magnetohydrodynamics code for astrophysical flows in two space dimensions. I - The hydrodynamic algorithms and tests. *ApJS* 80, 753–790.
- Takeuchi, T., Clarke, C. J., Lin, D. N. C., 2005. The Differential Lifetimes of Protostellar Gas and Dust Disks. *ApJ* 627, 286–292.
- Tanaka, H., Ida, S., 1996. Distribution of Planetesimals around a Protoplanet in the Nebula Gas. *Icarus* 120, 371–386.
- Tanaka, H., Takeuchi, T., Ward, W. R., 2002. Three-Dimensional Interaction between a Planet and an Isothermal Gaseous Disk. I. Corotation and Lindblad Torques and Planet Migration. *ApJ* 565, 1257–1274.
- Tanaka, H., Ward, W. R., 2004. Three-dimensional Interaction between a Planet and an Isothermal Gaseous Disk. II. Eccentricity Waves and Bending Waves. *ApJ* 602, 388–395.
- Udry, S., Mayor, M., Queloz, D., 1999. Towards a New Set of High-Precision Radial-Velocity Standard Stars. In: Hearnshaw, J. B., Scarfe, C. D. (Eds.), *ASP Conf. Ser. 185: IAU Colloq. 170: Precise Stellar Radial Velocities*, pp. 367.
- van de Kamp, P., 1963. Astrometric study of Barnard's star from plates taken with the 24-inch Sproul refractor. *Astron. Journal* 68, 515–521.
- Ward, W. R., 1981. Solar nebula dispersal and the stability of the planetary system. I - Scanning secular resonance theory. *Icarus* 47, 234–264.
- Ward, W. R., 1997. Protoplanet Migration by Nebula Tides. *Icarus* 126, 261–281.
- Wolf, S., Gueth, F., Henning, T., Kley, W., 2002. Detecting Planets in Protoplanetary Disks: A Prospective Study. *ApJ* 566, L97–L99.
- Wolszczan, A., 1991. Two Planets Around a 6.2-ms Pulsar 1257 + 12? *BAAS* 23, 1347.
- Ziegler, U., 1998. NIRVANA + : An adaptive mesh refinement code for gas dynamics and MHD. *Computer Physics Communications* 109, 111–134.

I would like to thank everyone who supported me over the last few years, in good times and in bad times. Over the last 3 years I have learned a lot not just about Astronomy and Physics but also about myself. Especially I would like to thank my parents for supporting me all this time, my colleagues at the Institute in Tübingen and especially Willy Kley who kept believing in me in tough situations. I would like to thank the European Union for making this Ph.D. possible by funding the RTN Planets Network (grant HPRN-CT-2002-00308). Finally thanks to Michał Różyczka for providing extra funding that allowed me to finish the project.

9 Curriculum Vitae

Personalialia

Name	Gerben Dirksen
Date of birth	June 19 th , 1979
Nationality	Dutch
E-mail address	dirksen@tat.physik.uni-tuebingen.de

Education

12/2002 - 4/2006	Ph.D. student in Astrophysics at Tübingen University under the supervision of prof. Kley. Thesis title: "Disk - Planet interaction: Eccentricity excitation and orbital evolution".
6/2002	Received M.Sc. degree in Astronomy at Leiden University. Thesis supervisor: dr. J. Luu. Title: "The dynamics of the outer Jovian satellites".
1996 - 2002	Undergraduate at Leiden University in Astronomy and Mathematics.
1990 - 1996	Gymnasium at the "VOS" in Vlaardingem, the Netherlands.

Work experience

1997 - 1999	Working for OGD installing computer hardware and software.
1998 - 2001	Student assistant for Linear Algebra and Calculus in Leiden.
2000 - 2002	Tutor in Mathematics and Physics for high school students.
2004 - 2006	Student assistant in Computational Physics in Tübingen.

Side activities

1986 - 1994	Active member of youth astronomy club JWG.
2000 - 2001	Secretary (2000) and Treasurer (2001) of student board game society "Het Duivelsei".
1999 - 2004	Represented the Netherlands and Germany in international youth Bridge.

Language skills

Fluent in Dutch, English and German